



TECHNISCHE
UNIVERSITÄT
WIEN

Vienna University of Technology

DIPLOMARBEIT

Significance of the spinal curvature in human transcutaneous spinal cord stimulation.

A computer modeling study.

Ausgeführt am Institut für
Analysis und Scientific Computing
der Technischen Universität Wien

unter der Anleitung von
Ao.Univ.Prof.i.R. Dipl.-Ing. Dr.rer.nat. Dr.sc.med. Dr.techn. Frank Rattay
Projektass. Dipl.-Ing. Mag. Dr.techn. Simon Michael Danner
und
Dipl.-Ing. Dr.techn. Karen Minassian

durch
Markus Müllner-Rieder
Barthgasse 7/11
1030 Wien

Wien, 5. Mai 2015

Unterschrift (Student)

Erklärung zur Verfassung der Arbeit

BSc Markus Müllner-Rieder
Barthgasse 7/11, 1030 Wien

Hiermit erkläre ich, dass ich diese Arbeit selbständig verfasst habe, dass ich die verwendeten Quellen und Hilfsmittel vollständig angegeben habe und dass ich die Stellen der Arbeit – einschließlich Tabellen, Karten und Abbildungen –, die anderen Werken oder dem Internet im Wortlaut oder dem Sinn nach entnommen sind, auf jeden Fall unter Angabe der Quelle als Entlehnung kenntlich gemacht habe.

Wien, 5. Mai 2015

Markus Müllner-Rieder

Acknowledgements

I thank Dr. Frank Rattay and Dr. Karen Minassian for the scientific support. Special thanks to Dr. Simon Danner for helpful discussions, scientific support and provided material.

Additional thanks to all proof-readers and people who gave me inspiration and motivation when creating this thesis.

Kurzfassung

Es wurde gezeigt, dass Rückenmarksstimulation (SCS) bei Menschen mit Rückenmarksverletzung die Gangart verbessern und die Spastizität verringern kann. Es gibt 2 übliche Methoden von SCS: Epidurale SCS welche implantierte Elektroden verwendet, und Transkutane SCS (tSCS), welche Oberflächen Elektroden verwendet. tSCS kann dieselben neuronalen Strukturen stimulieren wie epidurale SCS und wurde in mehreren Studien verwendet. Diese Studien haben in verschiedenen Körperpositionen stimuliert, was unterschiedlich gute Ergebnisse zur Folge hatte. Eine Ursache dafür könnte die Krümmung der Wirbelsäule sein. Da die Wirbel im Vergleich mit dem umgebenden Gewebe eine geringe Leitfähigkeit aufweisen können sie durch Verschiebung den Stromfluss durch den Wirbelkanal ändern, welches die Effektivität der Stimulation ändern kann.

In dieser Arbeit untersuche ich die Wirkung der Wirbelsäulenkrümmung auf die Effektivität von tSCS in einem Computermodell. Es wurde ein Zwei-Schritt Verfahren benutzt. Zuerst wurde die Potentialverteilung in einem menschlichen Torso mittels Volume-Conductor-Modell berechnet. Das Potential entlang Nervenfasern wurde aufgenommen und in einem Nervenmodell weiterverarbeitet. Dieses mathematische Modell berechnet die Anregungsschwelle und die Position an der ein Aktionspotenzial auftreten würde. Dies wurde für 3 verschiedene Positionen gemacht: Vorwärts gebeugt, Aufrecht und Rückwärts gebeugt. Als Geometrie wurde ein Modell eines menschlichen Torso erstellt, welches alle anatomischen Aspekte, die für die Messung von Biophysikalischen und Neurophysiologischen Prozessen in der Nähe des Rückenmarks nötig waren, beinhaltet.

Die Ergebnisse zeigen, dass sich der Stromfluss in vorgebeugter Position nach oben und unten aufteilt, während der Fokus nach unten liegt wenn man aufrecht oder zurückgebeugt ist. Das absolute Potential in der Rückenmarksflüssigkeit ist vorgebeugt am höchsten und nach hinten gebeugt am niedrigsten. Dies beeinflusst die Anregungsschwellen nicht, welche nach vorne gebeugt allgemein höher sind. Es ist möglich diese hohen Anregungsschwellen teilweise zu kompensieren indem man die Rückenelektroden cranial verschiebt.

Verglichen mit anderen Studien zeigt die aufrechte Position Werte im gleichen Bereich, daher sind das Modell und die verwendeten Parameter adäquat. Die Resultate zeigen, dass vorwärts die schlechteste Position ist und rückwärts die Beste. Die Position beeinflusst die Effektivität von tSCS maßgeblich und sollte daher immer beachtet werden.

Abstract

Spinal cord stimulation (SCS) has been shown to augment gait and reduce spasticity in individuals with spinal cord injury. There are 2 common methods of SCS: epidural SCS, which uses implanted electrodes, and transcutaneous spinal cord stimulation (tSCS), which uses surface electrodes. tSCS is able to stimulate the same neural structures as epidural SCS and was used in multiple studies. These studies used different body positions during stimulation, which showed varying effectiveness in the results. One reason could be the curvature of the spine. Vertebrae have a low conductivity compared to the surrounding tissue, therefore if they move they change the current flow through the spinal canal, which can change the effectiveness of the stimulation.

In this thesis, I studied the effect of spinal curvature onto the effectiveness of tSCS using a computer model. A two-step approach was used. First, the potential distribution generated by the stimulation was calculated in the human torso using a volume conductor model. Then the potential is evaluated along nerve fiber trajectories and used as the input for a nerve fiber model. This mathematical model calculates the excitation threshold and the position where an action-potential would occur. This is done for 3 different positions: leaning forward, upright and leaning backward. As geometry, a model of a human torso was created with all anatomical aspects needed for a measurement of the biophysical and neuro-physiological processes in the proximity of the spinal cord.

The results show that the current flow spreads up and down when leaning forward, but is more focused downward when being upright or leaning backward. The absolute potential in the cerebro-spinal fluid (CSF) is highest when leaning forward and lowest when leaning backward. This does not affect the excitation thresholds, which are overall higher when leaning forward. It is possible to partially compensate these high thresholds by moving the back electrodes cranial.

Compared to other computational studies the results for the upright position are in the same range, therefore the model and the used parameters are adequate. The results suggest that the worst position is leaning forward and the best position is leaning backward, although there is only a small difference between leaning backward and being upright. The position greatly influences the effectiveness of tSCS and should always be taken into account when using it.

Abbreviations

CAD computer-aided design. 30–35, 41

CNS central nervous system. 7, 13–15

CSF cerebro-spinal fluid. vii, 6, 7, 30, 35, 36, 38–40, 42, 47, 49–52, 61, 62

CSV comma-separated values. 31, 32, 42

CT computer tomography. 30, 32

MRI magnetic resonance imaging. 30, 32

PNS peripheral nervous system. 13

PRM posterior root-muscle. 24, 25

SCS spinal cord stimulation. vii, 1, 3, 25, 62

tSCS transcutaneous spinal cord stimulation. vii, 1–3, 23–27, 62–65

VBA visual basic for applications. 42

Contents

Kurzfassung	v
Abstract	vii
Abbreviations	ix
1 Introduction	1
2 Anatomical and Physiological Background	5
2.1 Spine & Spinal cord	5
2.2 Root fibers & Spinal nerves	7
2.3 Neurons & Action Potential	13
2.4 Extracellular stimulation and the activating function	16
2.5 Applications of transcutaneous spinal cord stimulation	24
3 Model	29
3.1 Volume Conductor Model	29
3.2 Nerve Fiber Model	42
4 Results	47
4.1 Results from the Volume Conductor Model	47
4.2 Results from the Nerve Fiber Model	51
5 Discussion	61
Bibliography	67
A Appendix	75

Introduction

Spinal cord stimulation (SCS) introduces electric current into the spinal cord to activate neural structures. There are 2 fundamental methods of SCS: implanted electrodes (epidural) and surface electrodes (transcutaneous). Implanted electrodes are inserted directly in the epidural space and show a high effectiveness. Surface electrodes are applied to the skin in a very fast and cheap way and can easily be removed without leaving a trace. Figure 1.1 shows skin electrodes placed in a setup similar to the one simulated in this thesis.

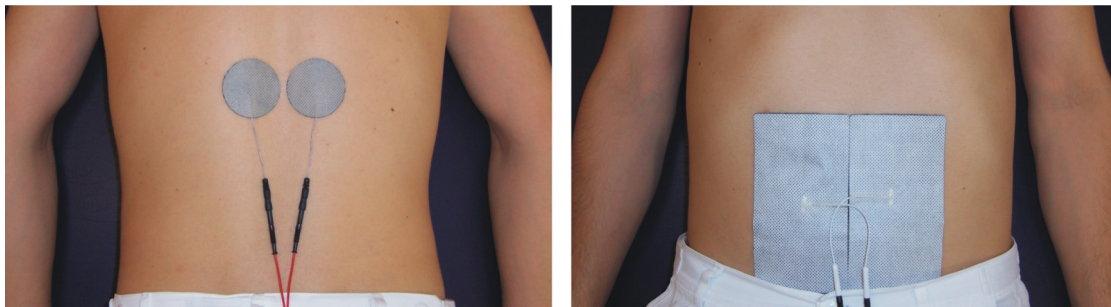


Figure 1.1: The placement of the electrodes during a study. The left figure shows the 2 back electrodes, the right figure the large stomach electrode. Source: Ladenbauer (2008)

Epidural SCS is able to help motor incomplete spinal injured patients to regain volitional control (Harkema et al., 2011; Angeli et al., 2014). Even though the stimulation is unfocused, transcutaneous spinal cord stimulation (tSCS) is able to selectively stimulate the same neural structures, the afferent fibers in the posterior roots (Minassian et al., 2007). This means that the fibers can be stimulated without stimulating neighboring

structures like the white and grey matter of the spinal cord and the afferent fibers which was also shown using computer simulation (Ladenbauer et al., 2010; Danner et al., 2011). Subsequently, it was shown that tSCS is able to modify the altered gait from spinal cord injuries (Hofstoetter et al., 2014a) and can be used to control the spinal spasticity (Hofstoetter et al., 2014b).

To develop a good treatment it is important to know the most effective way to apply the stimulation, which depends on different parameters like electrode type, size and placement, stimulus type, amplitude, frequency and length as well as body positions. But the threshold needed for stimulation differs when using different body positions. This was shown with epidural stimulation by Cameron and Alo (1998) and Olin et al. (1998). Computer simulations showed that the main reason is the distance between spinal cord and electrode (Holsheimer et al., 1995; Ross and Abejón, 2014), which changes when the patient changes body position (Holsheimer et al., 1994; Ranger et al., 2008). Figure 1.2 shows the position of the spinal cord in 2 different positions.

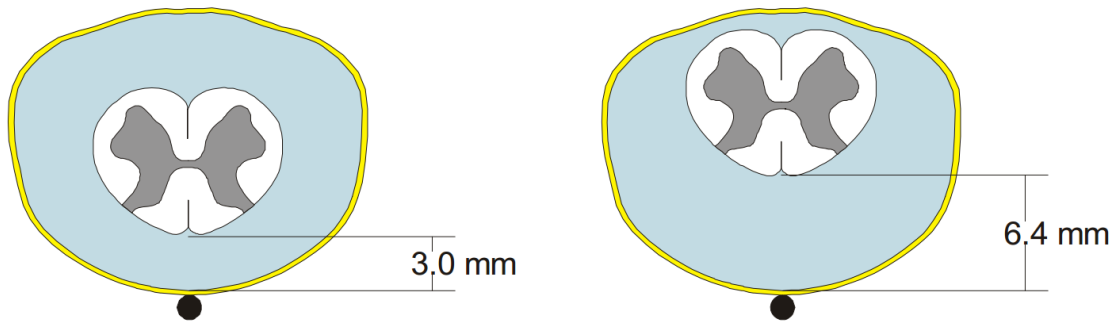


Figure 1.2: The position of the spinal cord in the spinal canal. Left: Supine position, Right: Prone position. Figure source: Rattay et al. (2002), Data source: Holsheimer et al. (1994)

Newer stimulation devices are able to adapt stimulation thresholds to body positions with good results (Schade et al., 2011; Schultz et al., 2012). Such devices do not exist for tSCS and there is no common recommendation about what body position should be used when doing different kinds of simulation studies. Therefore, current studies are carried out in many different positions like standing upright (Hofstoetter et al., 2014a), seated (Roy et al., 2012), semi-prone seated (Knikou, 2013) and supine (Minassian et al., 2007) which leads to mixed results. It was shown for example that responses are suppressed during stimulation in supine position (Minassian et al., 2007) but they are not modified when sitting semi-prone (Knikou, 2013).

It is hypothesized that the reason for the dependence on the body position in tSCS is the same as in epidural SCS: The position of the spinal cord in the spinal canal. The spinal cord shifts from ventral, when leaning forward, to dorsal, when leaning backward. It is also possible that the changes in the electric field in the vertebral column have a great influence on the stimulation threshold due to the general positions of the vertebrae. The aim of this thesis is to validate the empirically tested data by creating a computer simulation and also check if the excitation threshold and position depends on the position of the spinal cord in the spinal canal similar to Holsheimer et al. (1995).

Anatomical and Physiological Background

The anatomy and physiological parameters are very important when working with computer simulations. Many aspects of the anatomy have to be represented in the geometry for the simulation, and some key parameters have to be correct to get a representative model. The anatomy of the thorax and the conductivities for different tissues are the most important parts for the Comsol model. The most important parts for the nerve fiber model are the trajectories of the nerve roots after leaving the spinal cord, the model of the neuron stimulation itself and the nerve fiber diameter, which greatly influences the outcome of this simulation.

2.1 Spine & Spinal cord

The spine, or the vertebral column, houses and protects the spinal cord and provides stability to the body. It consists of 24 independent vertebrae and 9 fused vertebrae, which are named after their location. The first 7 in the neck (C1-C7) are called cervical vertebrae. The next 12 in the torso (TH1-TH12) are called thoracal vertebrae. The following 5 in the lower back (L1-L5) are called the lumbar vertebrae. These were the independent 24, the fused ones consist of 5 sacral vertebrae (S1-S5), which form the os sacrum, and 4 coccygeal vertebrae, which form the os coccyx. A single vertebra consists of bone and hyaline cartilage. The form of the vertebrae changes with the vertebral level, but all of them have a body, which is anterior, and a vertebral arch, which is posterior.

The bodies of the vertebrae are connected with intervertebral discs that enable movement of the vertebral column by building joints. The vertebral arch contains 2 pedicles, which are connected to the body, 2 laminae and 7 processes. It also features multiple facets, where the ribs and the adjacent vertebrae are connected. The spine is surrounded by multiple muscles, but 3 of them are important for the simulation: psoas major, quadratus lumborum and the erector spinae. A cross-section of these muscles can be seen in figure 2.1.

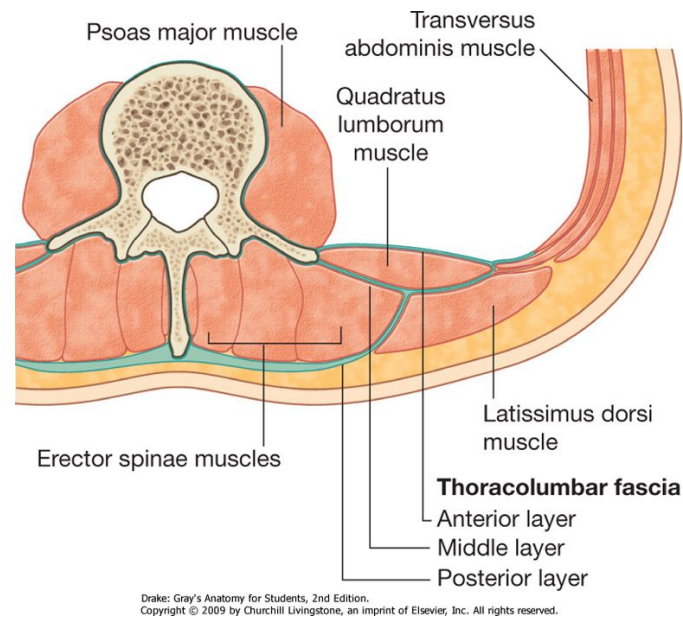


Figure 2.1: Transversal cross section of the torso showing the muscles surrounding the spine. Source: Drake (2010)

The space between the body and the arch is called vertebral canal. It is a bony canal that contains the epidural fat, the cerebro-spinal fluid (CSF), 3 layers of membranes, which are called spinal meninges, and the spinal cord. The task of the fat and the meninges is to protect the spinal cord and keep the CSF contained. The outermost layer is adipose tissue which is called the epidural fat. It contains capillaries to supply the spinal cord with blood, and it is soft to dampen shocks that would otherwise affect the spinal cord. Attached to the epidural fat is the dura mater, which also acts as a protection for the spinal cord. The highly conductive CSF lies between the dura mater and pia mater which are connected by the arachnoid mater. The spinal cord is attached to the arachnoid mater and the dura mater with denticulate ligaments.

The spinal cord is an extension of the nervous system coming from the brain's base. Along

its way, it has 2 enlargements: the cervical enlargement and the lumbar enlargement. Their function is to supply the upper and lower limbs with nerves. The spinal cord contains 2 different types of nervous tissue: grey matter in the middle and white matter on the outside. White matter consists mostly of myelinated axons. The myelin on the axons is responsible for its white color, while the capillaries give it a pink shine. Grey matter consists of cell bodies, dendrites, myelinated and unmyelinated axons and glia cells. The grey matter processes the information while the white matter connects different areas of grey matter.

2.2 Root fibers & Spinal nerves

Multiple nerve rootlets leave the spinal cord at every spinal cord segment dorsolaterally and ventrolaterally. These nerve rootlets combine to form the anterior and posterior root nerves. The posterior roots first combine into the spinal ganglion (dorsal root ganglion) which relays sensory information into the central nervous system (CNS). The output of the spinal ganglion then merges with the anterior root to form the spinal nerve. This means there are 4 root nerves per segment that finally combine to form 2 spinal nerves, one per side. The spinal nerves leave the vertebral canal through a lateral hole called intervertebral foramina, which resides between two vertebrae. Figure 2.2 shows that the level of exit from the spinal cord must not match the vertebral exit point. In the upper areas, the root nerves are relatively short, because they can immediately exit the spinal canal. In the lower areas, the root nerves are quite long to be able to reach their exit point. This exit point is where root nerves merge into spinal nerves. This can be seen in figures 2.3 and 2.4 at different angles. The root nerves are surrounded by CSF like the spinal cord. In most cases the posterior roots bring sensory information from the body to the spinal cord, while the anterior roots route the information from the spinal cord to the muscles.

The spinal nerves provide motor, sensory and autonomic signals to different parts of the body depending on the exit level. There are 31 pairs of spinal nerves which are named after the region of the spine where they exit the vertebral canal. There are 8 cervical, 12 thoracic, 5 lumbar, 5 sacral and 1 coccygeal pair. The spinal cord ends in the conus medullaris, which is between vertebral level L1 and L2. Below the conus medullaris lies the cauda equina, which is a bundle consisting of the sacral and lumbar root nerves. It ends in the os sacrum, where the last nerves spread into the lower limbs. A cross section of different levels of the cauda equina can be seen in figure 2.5.

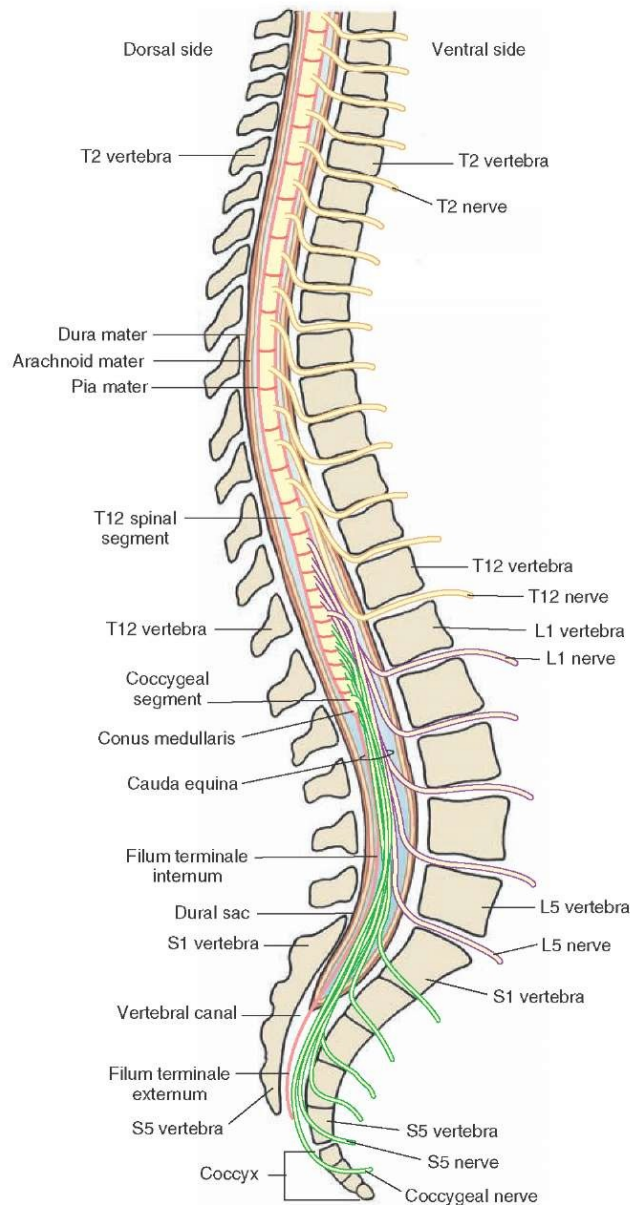


Figure 2.2: Sagittal cross section of the spine showing vertebrae, the spinal cord and spinal root nerves. This figure illustrates the distance between spinal exit level and vertebral exit level. It also shows that the spinal nerves exit below the corresponding vertebra (L1 nerve exits below L1 vertebra). This is only the case for T1 and lower. All cervical nerves exit above the corresponding vertebra. Source: Anatomy Body Gallery

► **Cross Section of the Spinal Cord, Showing Route Taken by Afferent and Efferent Axons**

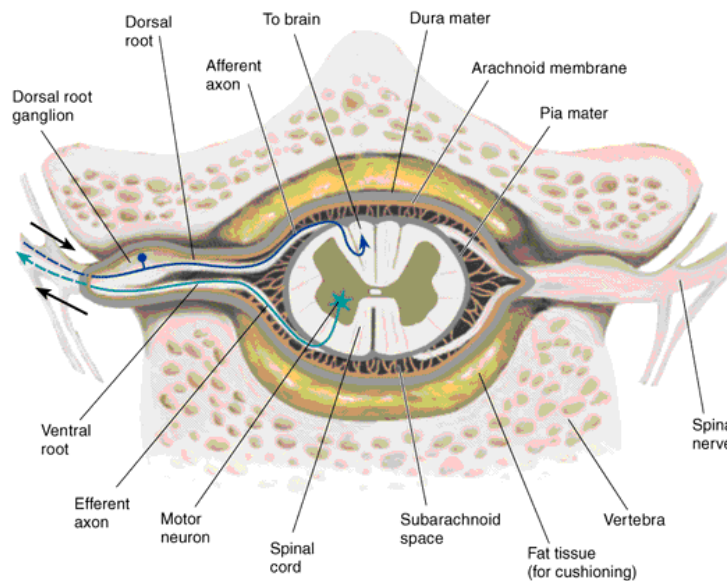
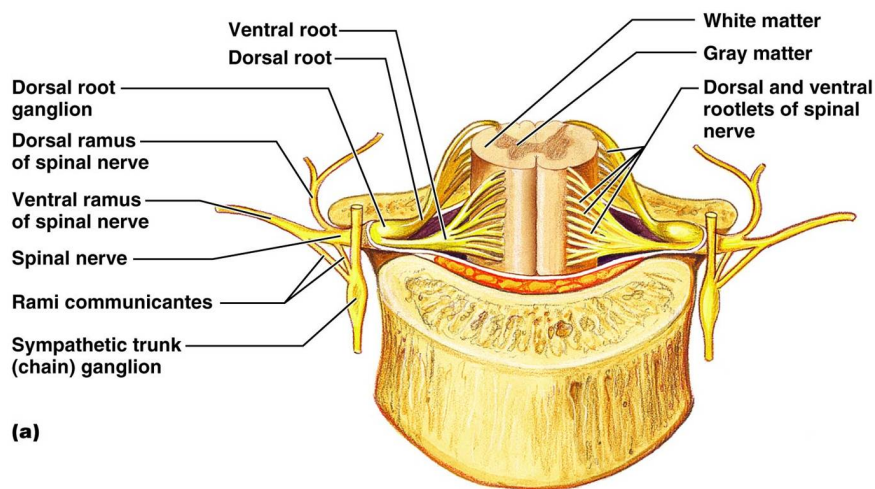


Figure 2.3: Transversal cross section of the spine showing important constructs in the vertebral canal. It also shows that the anterior and posterior roots merge directly after they leave the intervertebral foramina. Source: Salinas



Copyright © 2006 Pearson Education, Inc., publishing as Benjamin Cummings.

Figure 2.4: Transversal cross section of the spine and the spinal cord at different levels, exposing root nervlets. This figure shares most of the structures with figure 2.3, but it displays them at a semi-frontal angle, which shows the origin of the nerve rootlets and the sympathetic trunk, which would not be visible otherwise. Source: Judith Brown CPD

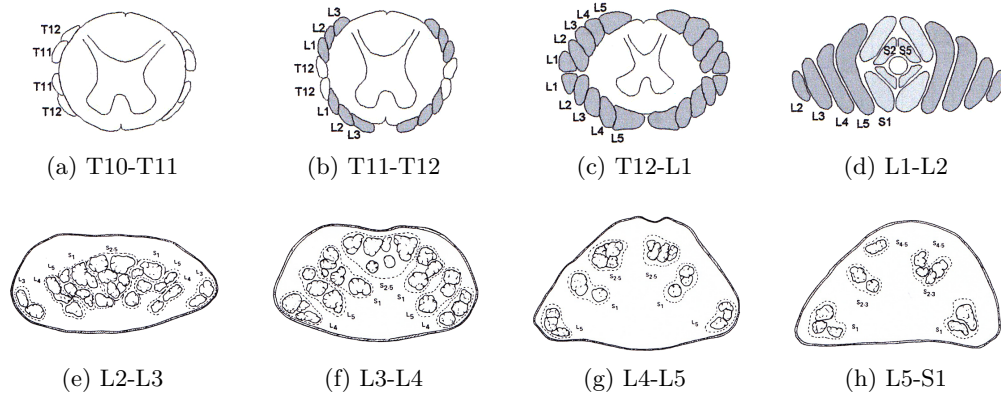


Figure 2.5: Cauda equina in different vertebral levels, which was acquired by fixation and dissection of human cadavers. Source of figure (a) to (d): Minassian (2000). Source of figure (e) to (h): Cohen et al. (1991).

This figure provides important information for modeling the root nerves, because it shows which nerves are present at which level and subsequently which have already left the pia mater. It also shows the position of single nerves that are positioned around the spinal cord when it is present. The next nerves to leave the dural sac lie to the far right and left and the last nerves lie at the top and the bottom (See figure 2.5, subfigure a to c). When the spinal cord is not present the first nerves to leave still lie to the far left and right, but the last nerves lie at the innermost part (See figure 2.5, subfigure d to h). The spinal cord is shorter than the spine, it does not extend along the whole vertebral column. This happens because the spinal cord isn't growing as fast as the bony structure around it. This means that the spinal cord segments are not equal to the vertebral segments. To model a starting point for the nerve roots, a mapping between these levels had to be found. This mapping was determined by multiple sources like Wall et al. (1990) and Lang and Geisel (1983). Figure 2.6 shows the data determined by Lang and Geisel (1983). Subfigure A shows the variations of the data and subfigure B shows the actual mapping derived from the data. The starting point was chosen to be halfway between the start and the end of each segment. The form of the start is shown in 2.7. The anterior nerve fibers leave the spinal cord straight, while the posterior nerve fibers leave it at an angle, roughly following the butterfly shape of the grey matter.

The last information that is missing to model the nerve roots is the horizontal progression. The problem is that there is no exact anatomical information about them in literature because they cannot be seen with optical methods and a dissection destroys the inner

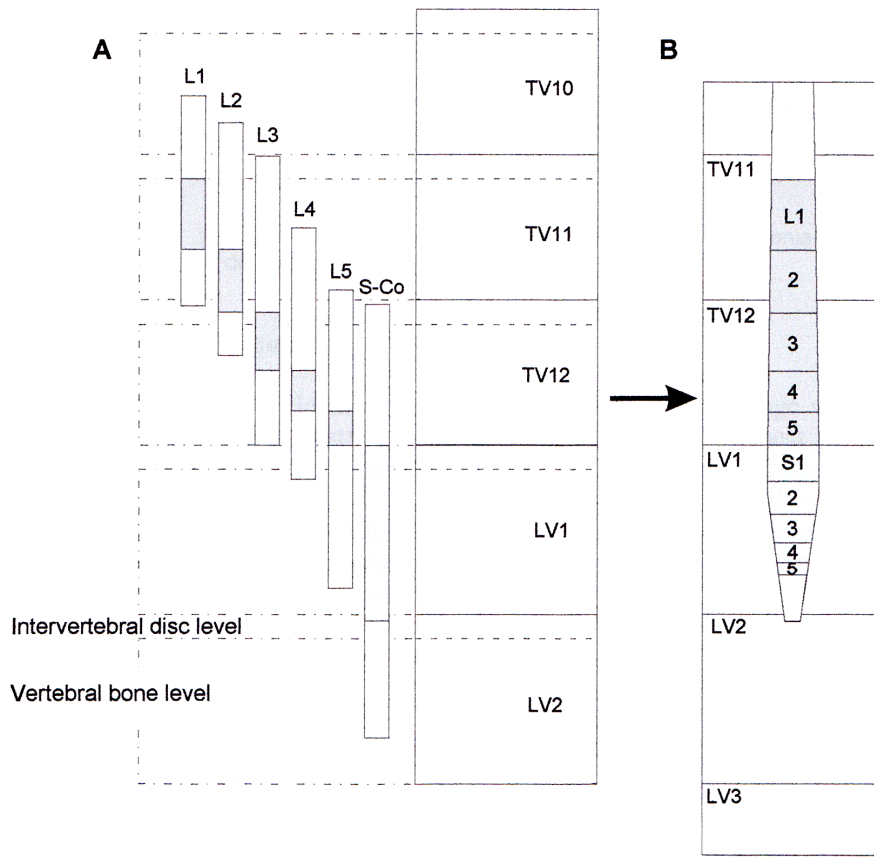


Figure 2.6: Mapping from vertebral levels (A) to spinal levels (B). Used to determine the point where the nerve root exits the spinal cord. Source: Minassian (2000)

composition of these structures. Minassian (2000) has derived the trajectories of the nerves by combining multiple methods. He combined data from Wall et al. (1990) and Hasegawa et al. (1996) with information from anatomists and anatomical photographs to get the trajectories which can be seen in figure 2.7.

The figure shows that the fibers bend immediately downward. The anterior and posterior root merge when they leave the dural sac. The point where they merge is more frontal, therefore the posterior root nerve has to be at an angle to meet the anterior nerve. When they leave the dural sac, they have a specific angle that depends on the vertebral segment. This means 2 additional sources of information had to be used to model it correctly. Lang (1984) gives the length of each nerve fiber L1-S1 in cm before leaving the dural sac. With this information it can be derived where each nerve leaves and when the angle

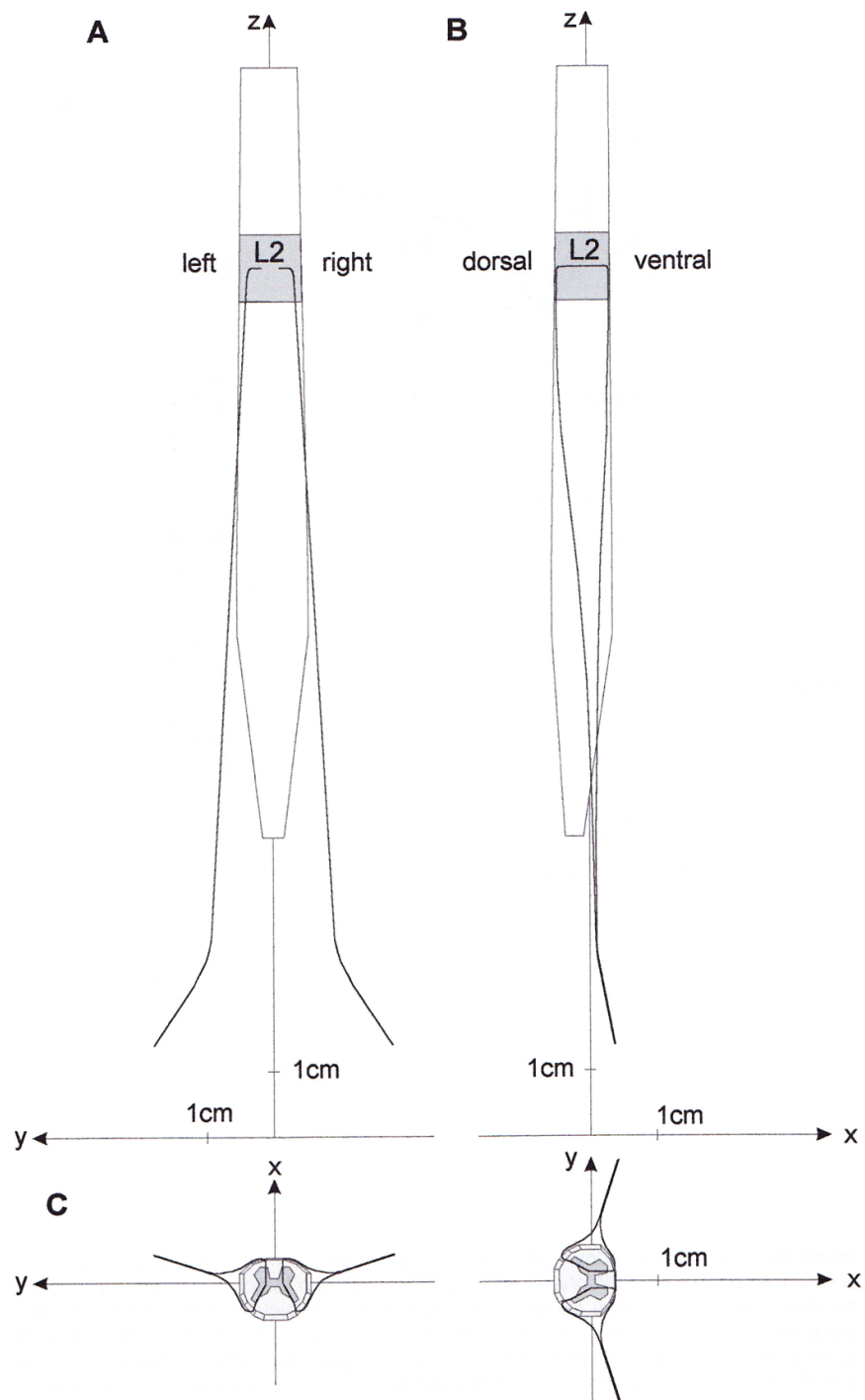


Figure 2.7: Trajectories. Source: Minassian (2000)

should be applied. Hasegawa et al. (1996) contains the angles of the L1-S1 root nerves after they leave the dural sac.

2.3 Neurons & Action Potential

The nervous system can be classified in multiple ways. First in the CNS, which consists of the brain and the spinal cord, and the peripheral nervous system (PNS), which consists of the nerves beginning at the spinal cord. The PNS can be split into the voluntary nervous system, which contains the motor neurons we can actively activate, and the autonomic nervous system, which we can't influence. The autonomic nervous system can be split into sympathetic nervous system, parasympathetic nervous system and the enteric nervous system. The entire nervous system consists of 2 types of cells: neurons, which do the signal processing and transfer, and the glia cells, which provide support and protection to the neurons.

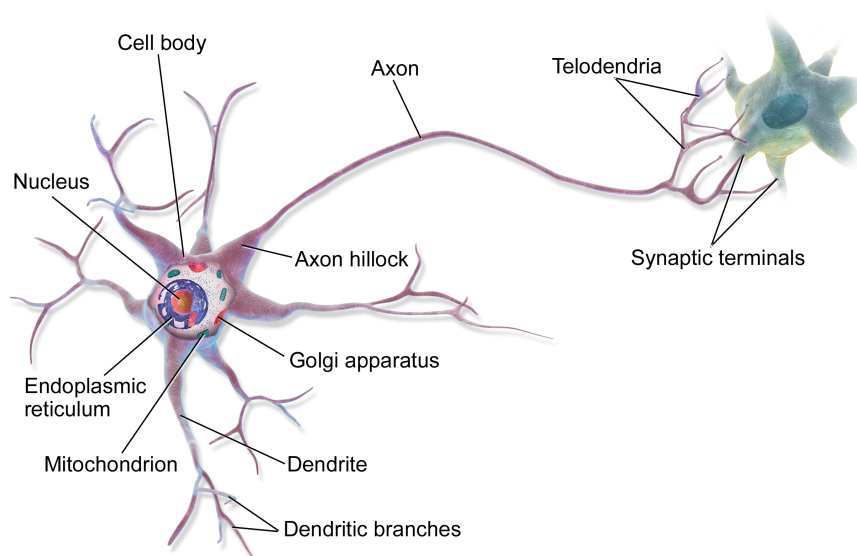


Figure 2.8: The structure of a neuron. Source: Blausen Medical

The neurons are the main method of signaling in the body. They route muscle activation signals from the brain to the body and carry sensory information back to the brain. They do this by generating action potentials, which are rapid changes in the cell membrane potential. The structure of a neuron can be seen in figure 2.8. The neuron consists of 4 distinct parts: The soma, which is the cell body, the dendrites, the axon and the axon terminals (presynaptic terminals). The soma contains the cell's nucleus and is

the metabolic center where the protein synthesis takes place. 2 Types of extensions are attached to the soma: One axon and multiple dendrites. The axon is a long structure that acts as the output of the neuron by carrying electrical signals from one neuron to the next one. Even though a neuron usually only has one axon, this axon may branch extensively and therefore can reach a lot of target neurons.

Dendrites on the other hand are the input of the neuron. There are usually multiple dendrites that branch out again in a tree like fashion enabling it to receive signals from a large amount of other neurons. The presynaptic terminal is at the outer end of the axon. It uses electrochemical signals to carry action potentials to the next neuron. The distance between the presynaptic and postsynaptic terminals is called synapse, which can be overcome by neurotransmitters like serotonin. Neurons can be classified by either polarity or direction. They can be unipolar, where one branch is dendrite and axon at the same time, bipolar, where one dendrite and one axon are apart and multipolar, where multiple dendrites and one axon are present. When classifying by direction they can be afferent, carrying information from the body to the CNS, efferent, routing signals from the CNS to the muscles and interneurons, when they connect different parts of the CNS.

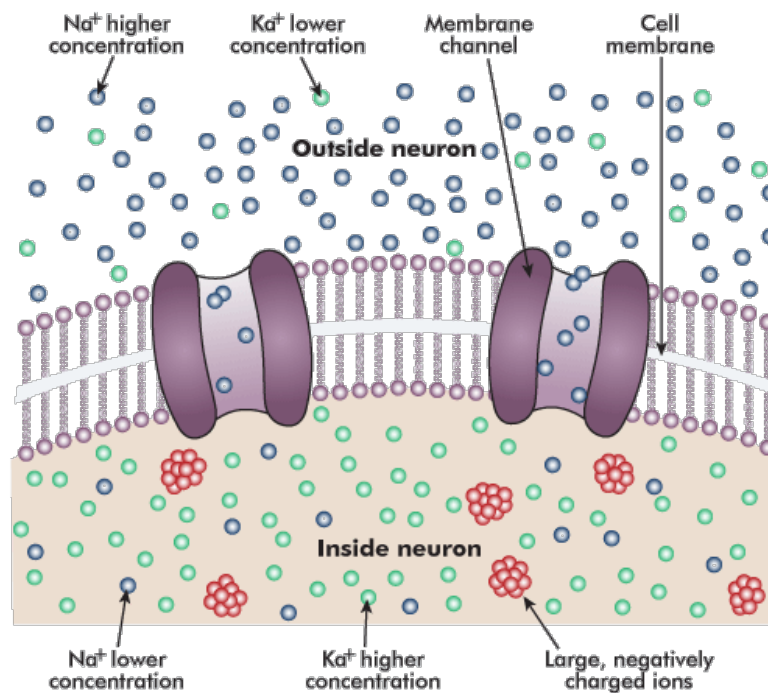


Figure 2.9: The structure of a neuron cell membrane. Source: WestOne Services

The main methods of signal transduction are called action potential and neurotransmitter.

A voltage difference is created by the cell's plasma membrane by allowing ions to pass through it. This is possible because specific proteins are embedded in the membrane, which act as voltage-gated ion channels. A graphical representation of a cell membrane can be seen in figure 2.9. The resting potential is usually -70 mV . An action potential is generated when the membrane is depolarized to about -55 mV . When this happens, the sodium channels open, allowing sodium into the cell, which increases the potential difference even more up to a maximum of about 50 mV . When the maximum is reached the sodium channels close and the potassium channels open, which allow it to repolarize to the resting potential. This causes a small hyperpolarization where the potential is, for a short time, smaller than the resting potential. This is important because it inhibits another stimulus, which makes it impossible that the signal travels back to where it started. (Kandel et al., 2000)

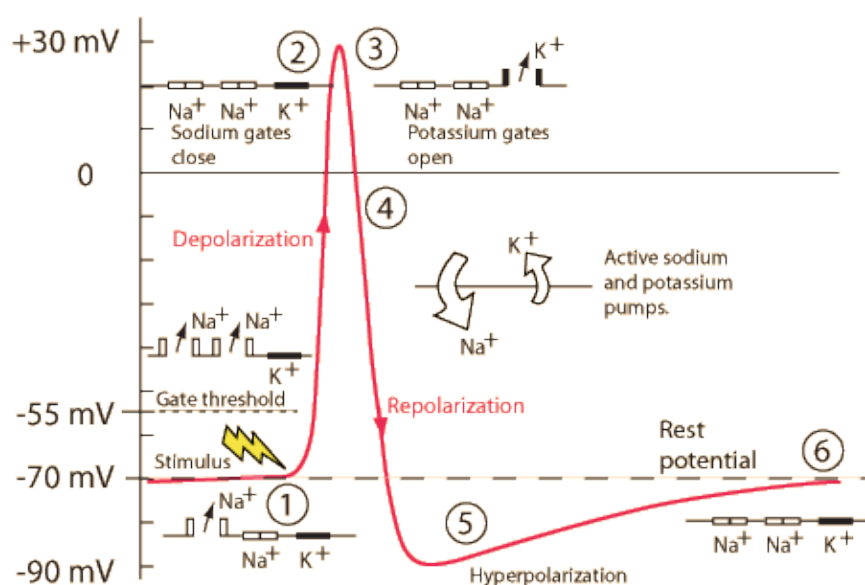


Figure 2.10: The generation of an action potential. Source: Charand

In order to propagate the action potential faster and with smaller losses the axon is surrounded by myelin, which has a high resistance and acts as insulator. The myelin is produced by specialized cells, which can be the Schwann cells in the periphery or oligodendrocytes in the CNS. This myelin sheath is only interrupted at the nodes of Ranvier, which mark the end of one myelin producing cell and the beginning of the next. The process of generating an action potential can be seen in figure 2.10.

When different structures of neurons were analyzed it was found that the most excitable

structure is the myelinated axon. In contrast, the excitability near a soma is low, (Porter, 1963; Nowak and Bullier, 1998; Rattay, 1998, 1999) because the soma has a high capacitance. Large nerve fibers have a lower threshold than thinner fibers and myelinated fibers have a lower threshold than unmyelinated fibers (Ranck, 1975; Rattay, 1987, 1990; Roth, 1994). The relation between fiber diameter and threshold is not linear, the thresholds increase faster with smaller size (Veltink et al., 1988; Struijk et al., 1993b). Usually, an axon is excited by a sudden change of external potential, because the activating-function anticipates a low threshold when the second order derivative of the potential is high (Rattay, 1998, 1999).

2.4 Extracellular stimulation and the activating function

The source of information in this section was, unless noted otherwise, Rattay et al. (2003). When looking at extracellular stimulation one of the biggest achievements was the understanding of the action potential. This was mainly the work of Hodgkin and Huxley (Hodgkin and Huxley, 1952), because they measured the response of a squid axon. They simplified the measurements by only taking a short part of the axon and using an electrode that was nearly as long as the axon part. In that way they blocked the complicated propagation mechanisms by providing the same voltage to every part of the axon. This can be seen in figure 2.11. They found out that the current from the stimulation divides in two parts: One is used to charge the capacitive membrane, and the other part passes through ion channels. This leads to the formula:

$$I_{stimulus} = C_m \frac{dV}{dt} + I_{ion} \quad (2.1)$$

where C_m is the capacity of the membrane, $I_{stimulus}$ is the current induced by stimulation and I_{ion} is the current that passes through ion channels. I_{ion} can be calculated by using membrane models. This equation can be transformed to get the rate of voltage change in the membrane:

$$\frac{dV}{dt} = [-I_{ion} + I_{stimulus}] / C_m \quad (2.2)$$

The stimulus current has to be high enough to induce more than the threshold voltage,

which leads to an opening of voltage-gated sodium channels. This leads to a sodium current, which causes the action potential without the need for further stimulation.

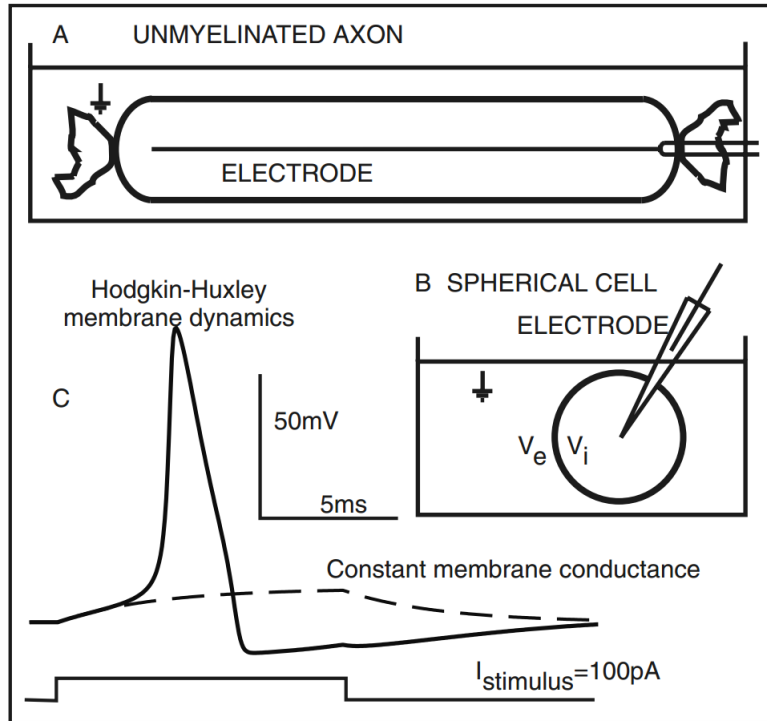


Figure 2.11: A and B show 2 different techniques to cause the same voltage for every part of the membrane. In subfigure A, an uninsulated wire is inserted into an unmyelinated nerve fiber. The length of the wire is approximately the same length as the nerve fiber. Subfigure B shows a spherical cell in a conductive medium. Subfigure C shows the result of a simulation of the Hodgkin-Huxley model with original data on a spherical cell. The dashed line shows the course if the membrane conductance would be constant and the black line shows it with Hodgkin-Huxley membrane dynamics. Source: Rattay et al. (2003)

In reality, the excitation process is not as easy as described, because current changes in one part of a nerve influence the adjacent parts, which leads to spike propagation. Therefore, compartment models were created, which divide nerves into multiple compartments interacting with another. Figure 2.12 shows the simulation results of a stimulated cochlear neuron using a compartment model. There are usually different types of compartments like axon, dendrite, soma, terminal and others. One of these compartment models is the compartment model for a myelinated nerve fiber, created by McNeal in 1976 (McNeal, 1976). This model is particularly interesting when trying to find the threshold and place of action potential initiation. The model can be analyzed with different methods, like linear equations or with more effort by solving differential equations. This means the

same aspects like complicated ion channel mechanisms can be neglected in order to gain speed during calculation. In this model, the sub-threshold membrane is modeled with constant conductance, which means the ion channel dynamics are omitted. Even then the model is able predict important mechanisms like the difference between anodic and cathodic or the influences of geometrical changes (Coburn, 1989; Rattay, 1990).

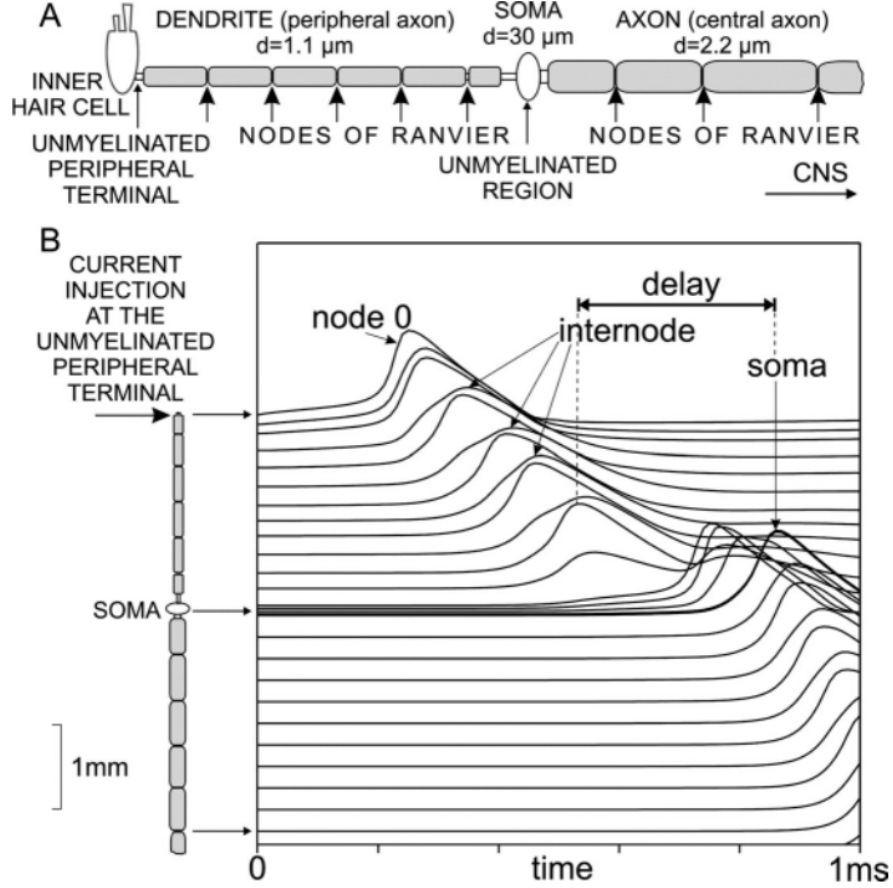


Figure 2.12: A shows a human cochlear neuron from nerve cell to axon. A stimulation of the unmyelinated peripheral end is simulated. The result of the simulation is shown in subfigure B. The lines are shifted so that they show their real location on the neuron. The soma introduces a relatively big delay on the signal. Details and Source: Rattay et al. (2003)

To model a cell membrane, a correlation between voltage and ion concentrations has to be found. This can be done by using Ohm's law and the Nernst equation.

$$E_m = \frac{RT}{zF} \ln \frac{c_e}{c_i} \quad (2.3)$$

E_m is the membrane voltage, c_e is the external ion concentration and c_i is the internal ion concentration. The term RT/zF consists of the gas constant, the temperature in Kelvin, the valence and the Faraday constant. This term is evaluated to 25 mV at 20 °C. When the voltage is known, the ratio between inside and outside concentrations can be calculated. This is 6 for sodium and 26.5 for potassium. This means that the sodium concentration outside is 6 times higher than inside. This approach is only valid if one type of ion is used. The Goldman equation is able to calculate the membrane voltage using K^+ , Na^+ and Cl^- ions.

$$E_m = \frac{RT}{F} \ln \frac{P_K[K]_e + P_{Na}[Na]_e + P_{Cl}[Cl]_i}{P_K[K]_i + P_{Na}[Na]_i + P_{Cl}[Cl]_e} \quad (2.4)$$

where $[K]_e$, $[Na]_e$ and $[Cl]_e$ are the external concentrations, $[K]_i$, $[Na]_i$ and $[Cl]_i$ are the internal concentrations and P_K , P_{Na} and P_{Cl} are the permeabilities per ion type, which are measured as speed (cm/sec). The internal and external concentration of chloride is switched, because it is a cation instead of an anion. The result of this equation is about -70 mV when the membrane is in resting state. Multiple cell membrane models were created, like the Hodgkin-Huxley model (Hodgkin and Huxley, 1952), which is derived from a nonmyelinated squid axon, the Frankenhaeuser and Huxley model (Frankenhaeuser, 1960) from a myelinated frog axon, the CRRSS model (Chiu et al., 1979) from a myelinated rabbit nerve node, the Schwarz-Eikhof model (Schwarz and Eikhof, 1987) from rat nodes or the SRB model (Schwarz et al., 1995) from human nerve fibers. An example of a compartment model can be seen in figure 2.13.

A compartment model consists of elements (compartments), which form an electrical network. There are many different compartment models with varying complexity. For example, if the surface area is considered a 3D model consisting of cylinders and spheres can be used, or they can just be included by using different factors for them. Another complexity is the inclusion of internode membrane currents. They are omitted many times, but can be approximately included by scaling the membrane capacity with the inverse of the number of myelin layers (Rattay, 1999). Current injection can be simulated by inducing the current directly in a compartment and setting all external potentials to 0, or by using the external potentials to induce these currents. If a current is induced in a compartment it must leave through either the left or the right adjacent compartment. If we extend equation 2.1 with this statement by using Kirchhoff's law we get:

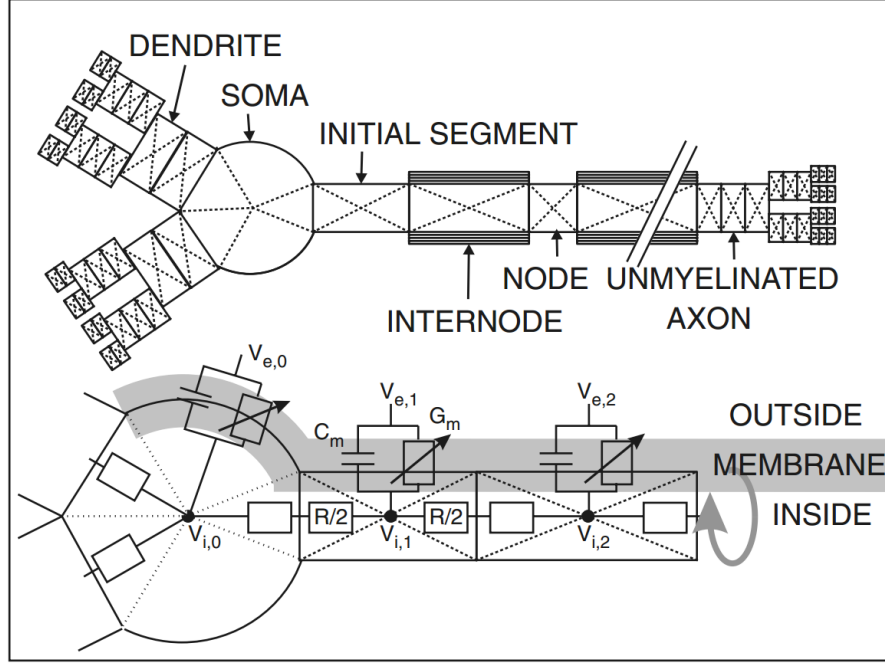


Figure 2.13: Example of a compartment model of a neuron with different compartment types. Source: Rattay et al. (2003)

$$I_{injected,n} = C_n \frac{d(V_{i,n} - V_{e,n})}{dt} + I_{ion,n} + \frac{V_{i,n} - V_{i,n-1}}{R_n/2 + R_{n-1}/2} + \frac{V_{i,n} - V_{i,n+1}}{R_n/2 + R_{n+1}/2} \quad (2.5)$$

where n is the index of the compartment, V_i is the internal voltage, V_e is the external voltage and R is the resistance of the compartment. When using the reduced membrane voltage $V = V_i - V_e - V_{rest}$ a system of differential equations evolves for calculating the voltage change:

$$\frac{dV_n}{dt} = \left[-I_{ion,n} + \frac{V_{n-1} - V_n}{R_{n-1}/2 + R_n/2} + \frac{V_{n+1} - V_n}{R_{n+1}/2 + R_n/2} + \dots \right. \\ \left. + \frac{V_{e,n-1} - V_{e,n}}{R_{n-1}/2 + R_n/2} + \frac{V_{e,n+1} - V_{e,n}}{R_{n+1}/2 + R_n/2} + \dots + I_{injected,n} \right] / C_n \quad (2.6)$$

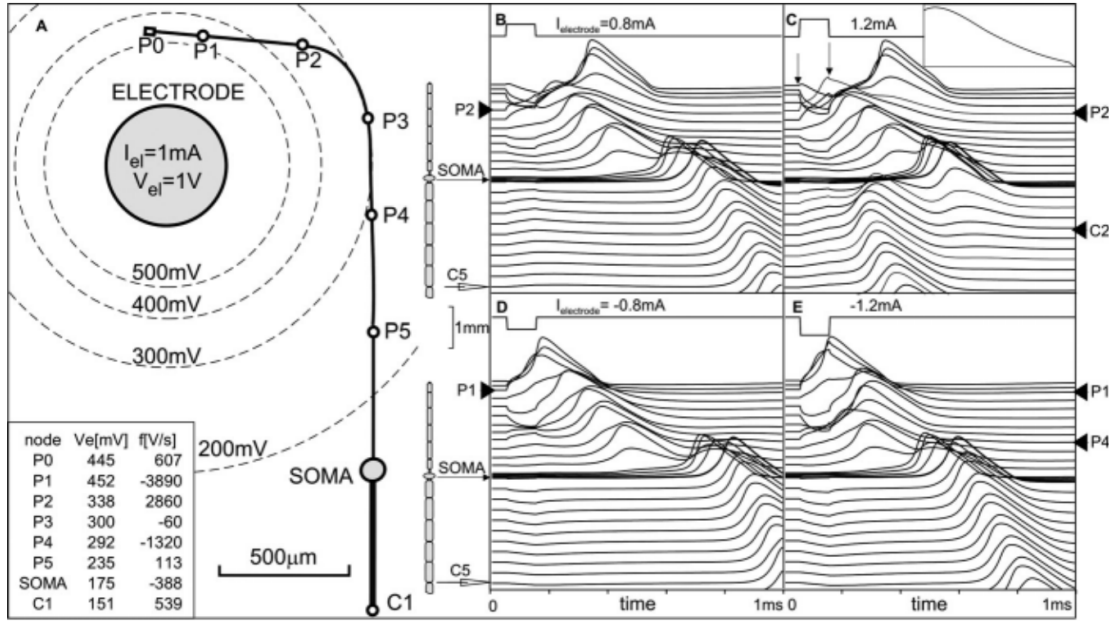


Figure 2.14: This figure shows the response when stimulating a human auditory nerve with a cochlear implant. The neuron is essentially the same as in figure 2.12. A shows the position of the electrode in relation to the nodes and the soma. The values of the activating function in the table are proportional to the slopes when the stimulus begins in B and C. B to E show the membrane voltages of all nodes over time, for different stimulus currents. The first arrow in C marks the stimulus onset and the second arrow marks the spike initiation at node P2. The spike is generated at P2 because the activating function is the biggest. B and C show anodic stimulation, D and E show cathodic stimulation. Source: Rattay et al. (2003)

The most important factor of the external potential per compartment is called the activating function.

$$f_n = \left[\frac{V_{e,n-1} - V_{e,n}}{R_{n-1}/2 + R_n/2} + \frac{V_{e,n+1} - V_{e,n}}{R_{n+1}/2 + R_n/2} + \dots \right] / C_n \quad (2.7)$$

Its unit is V/sec or mV/msec and it represents the speed of the membrane voltage change that is created by an external stimulus. If it is positive, a spike may be induced, if it is negative, hyperpolarization occurs. When looking at the activating function in experiments like the one shown in figure 2.14 it predicts that excitation is easier when stimulating with cathodic currents. As described before, McNeal created the first compartment model, where the solution can be calculated in an efficient way. He

simplified the internode membrane by setting the membrane conductance and capacity to 0. This reduces equation 2.6 to:

$$\frac{dV_n}{dt} = \left[-i_{ion,n} + \frac{d\Delta x}{4\rho_i L} \left(\frac{V_{n-1} - 2V_n + V_{n+1}}{\Delta x^2} + \frac{V_{e,n-1} - 2V_{e,n} + V_{e,n+1}}{\Delta x^2} \right) \right] / c \quad (2.8)$$

where d is the fiber diameter, Δx is the distance from node to node, ρ_i is the resistivity of axoplasm and L is the node length (Rattay, 1989, 1999). The ion current per node $i_{ion,n}$ and the membrane capacity c are per cm^2 . The formula of the activating function is now

$$f_n = \frac{d\Delta x}{4\rho_i L c} \frac{V_{e,n-1} - 2V_{e,n} + V_{e,n+1}}{\Delta x^2} \quad (2.9)$$

with $\Delta x \rightarrow 0$ follows:

$$f = \frac{d}{4\rho_i c} \frac{\partial^2 V_e}{\partial x^2} \quad (2.10)$$

One thing that can be seen in the formula is that the activating function is proportional to the diameter, which supports the measurements that conclude that thick axons are easier excitable than thin axons (Blair and Erlanger, 1933; Rattay, 1986). Another thing that can be seen is that the activating function is proportional to the second order spatial derivative of the electric potential on the nerve fiber. This means that the fiber trajectory through the electric field and the different mediae will greatly influence the nerve fiber excitability. The excitability can be influenced in both ways by the trajectory: Either it hinders an excitation by increasing the activation threshold or it supports an excitation by lowering the activation threshold. The following factors increase the excitability:

- When fibers bend convexly in relation to the cathode
- When fibers traverse from a high conductive to a low conductive medium, from the cathodes' view
- When fibers branch away from the cathode

The exact opposites of these factors lead to a decrease in excitability (Danner et al., 2014). Various computer simulations confirm that these factors highly influence the ability to activate spinal neural structures when using tSCS (Ladenbauer et al., 2010; Danner et al., 2011). Several hot spots were identified where the depolarization is maximal:

- Where the posterior rootlets enter the spinal cord
- Where the posterior and anterior roots exit the spinal cord
- Where the posterior column fibers branch

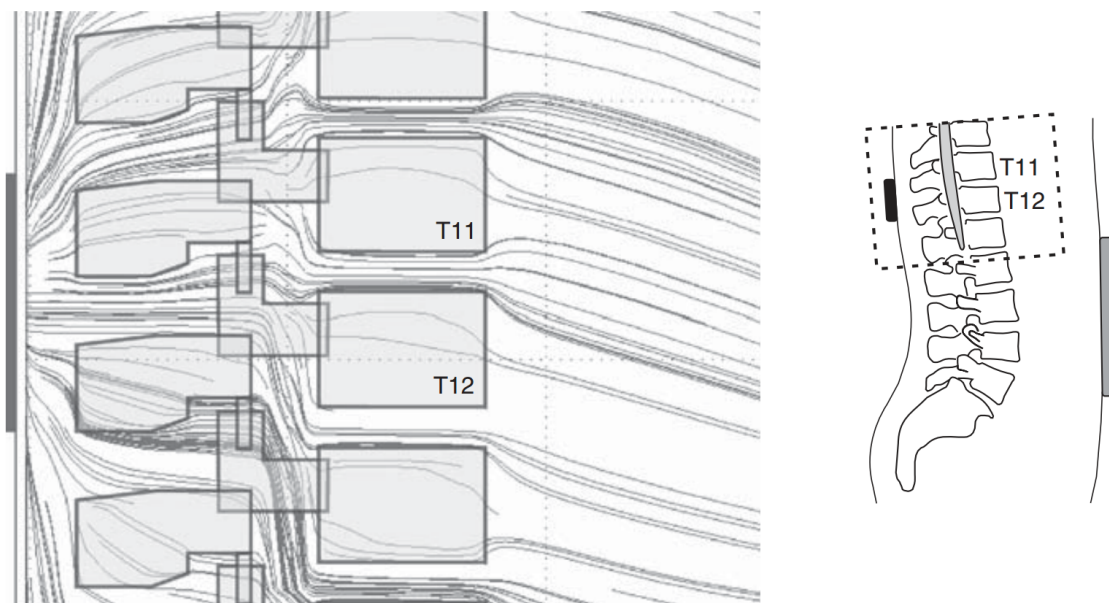


Figure 2.15: Sagittal cross-section of the current flow through a model of a human torso. A stimulating electrode was placed between T11 and T12, a ground electrode was placed on the stomach. Figure only shows the vertebrae and electrodes. The current avoids low conductivity tissues like the vertebrae and enters through more conductive tissues like the muscles or intervertebral discs. Source: Minassian et al. (2012) Details: Ladenbauer et al. (2010)

Figure 2.15 shows the simulated current flow through a human torso. Simulations have shown that structures in the spinal canal are activated in a specific order when the intensity is increased (Danner et al., 2014). Posterior root fibers are excited more easily than anterior root fibers because the trajectory of the anterior fibers is different when the spinal cord ends. When anterior root fibers exit the spinal cord, their orientation with respect to the electric field has a negative influence on the threshold when using cathodic

stimulation. Also, the posterior column fibers have a higher threshold than the posterior root fibers, because they lack substantial changes (Danner et al., 2011). The posterior column fibers in the white matter in the spinal cord itself are the intraspinal structures with the lowest threshold (Holsheimer, 2002), but have still the highest threshold of all structures listed here. Therefore, it can be assumed that neural structures in the spinal cord cannot be directly stimulated Minassian et al. (2012).

2.5 Applications of transcutaneous spinal cord stimulation

The source of information in this section was, unless noted otherwise, Minassian et al. (2012). Epidural spinal cord stimulation is used to modify impaired motor activity in humans. This is done by placing electrodes over the lumbar spinal cord to stimulate afferent fibers of posterior roots. These stimulations activate circuitries that activate muscles, which are otherwise not accessible when the spinal cord is injured. These muscle twitches that happen with every stimulus can be electromyographically recorded as compound muscle action potentials (Minassian et al., 2004). This can also be done by using a non-invasive technique called transcutaneous spinal cord stimulation (Dimitrijevic et al., 2004; Minassian et al., 2007). It can be applied in the same fields as epidural stimulation like motor control studies and gait modification.

There are several possible electrode setups when using tSCS. The method used in this thesis uses stimulating electrodes placed on the lower back and lower abdomen. This method is able to create reflexes in lower limb muscles in subjects with intact nervous system (Minassian et al., 2007; Hofstoetter et al., 2008) and subjects with impaired (motor complete or incomplete spinal cord injury) nervous system (Minassian et al., 2010). Even though the vertebrae have a low conductivity, other structures such as the intervertebral discs do not. This means that the spinal canal is not electrically shielded and that current can flow between the electrodes through the spinal canal. As described in the last chapter, the nerve roots in the vertebral canal can be stimulated if low threshold areas like the bend, which occurs directly after leaving the spinal cord, is reached. Figure 2.16 shows that responses evoked by tSCS show a similar morphology as the PRM reflexes created by epidural stimulation. These similarities show that tSCS is able to stimulate at least a subset of the same structures as epidural spinal cord stimulation.

By using tSCS it is possible to alter impaired motor activity, for example by modifying

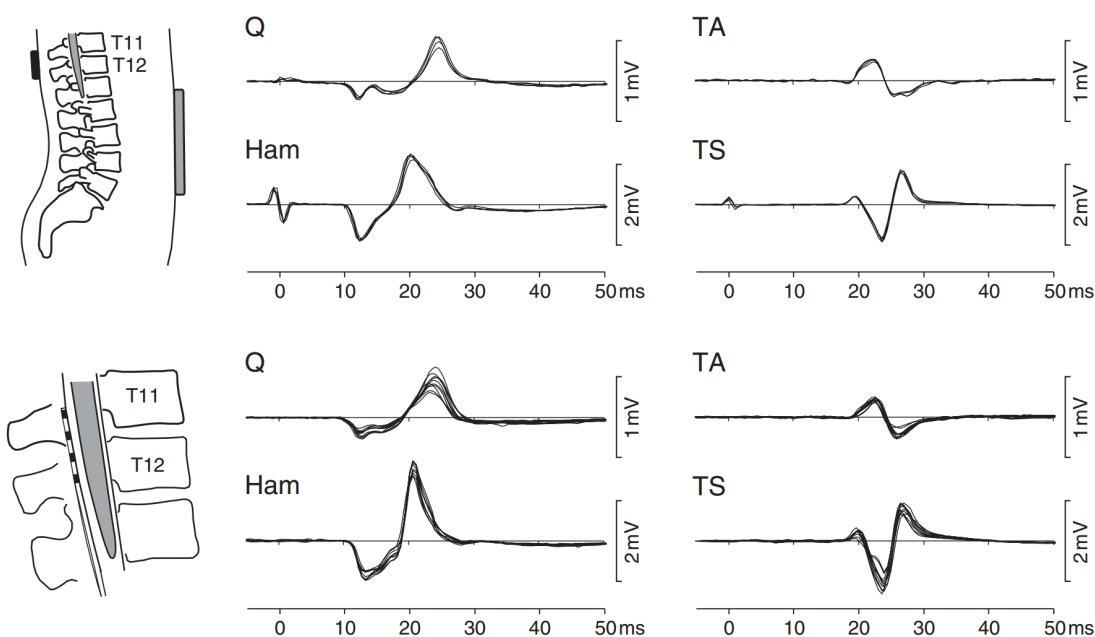


Figure 2.16: This figure shows the posterior root-muscle (PRM) reflexes resulting from epidural SCS (top) and tSCS (bottom). The 4 types of recorded muscle responses are from quadriceps (Q), hamstrings (Ham), tibialis anterior (TA) and triceps surae (TS). The data was gathered in a single session and the subject was an incomplete spinal cord injured patient. Source: Minassian et al. (2012)

lower limb spasticity. This was tested by Minassian et al. (2012), who recorded the voluntary and reflex functions before and after stimulation for 30 minutes. The subject was a 32 year old male who had a spinal cord injury 12 years prior. The skin electrodes were placed over the T11-T12 spinous process. The best positioning of the electrodes was determined by applying single stimuli and recording the PRM reflexes from multiple sites. To test if the afferent posterior roots were stimulated, the response to double stimuli was recorded. After these checks, the stimulation was set to a continuous stimulus of 50 Hz. The start intensity was 0 V and was slowly increased to accommodate the subject to the stimulation. The increase of intensity was stopped when paraesthesiae were induced in most lower limb dermatomes but the threshold of PRM reflexes was not reached. This intensity was applied for 30 minutes. Before the stimulation, the subject was asked to do specific tasks while the muscle responses were recorded. After the stimulation, the same tasks were recorded again. Previously, the movements evoked passive responses in other muscles, but after the stimulation these responses were reduced by a large amount. Also 2 10-meter walk tests with two crutches was performed, where the time improved

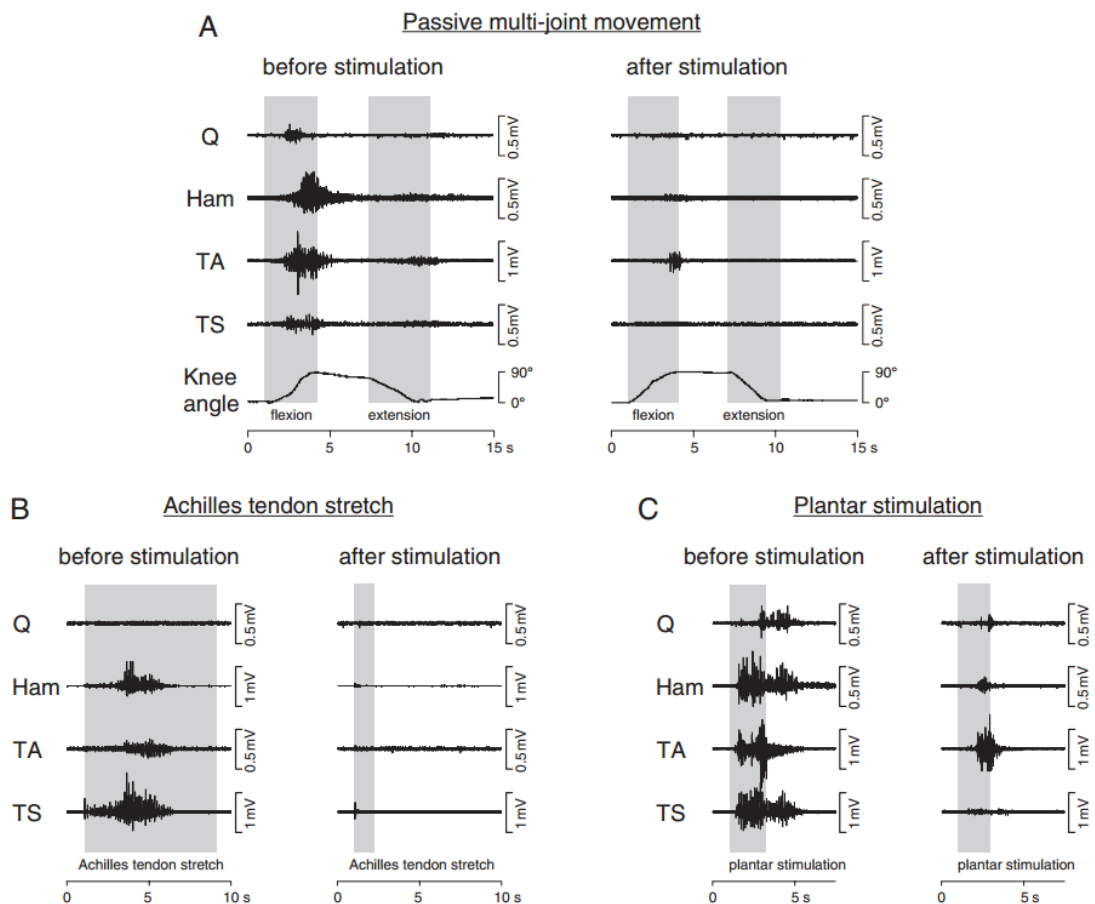


Figure 2.17: Electrophysiological data gathered from a spinal cord injured individual before and after spinal cord stimulation. These were recorded on quadriceps (Q), hamstrings (Ham), tibialis anterior (TA) and triceps surae (TS). Subfigure A shows a passive hip and knee flexion and extension movements. Subfigure B shows an Achilles tendon stretch and subfigure C shows plantar stimulation with a rod. All figures show that the spastic movements during passive movement and reflex triggering are much better than without stimulation. Source: Minassian et al. (2012)

from 49 and 54 seconds to 32 and 35 seconds. The results of some tasks performed by the patient can be seen in figure 2.17

Another use of tSCS is to improve neural control of locomotion. This was tested by Minassian et al. (2012) on a 28 year old female who had a spinal cord injury 10 years prior. The subject was tested on a treadmill while stepping without help from therapists or body-weight support. tSCS was used in a standing position with 30 Hz. The stimulation

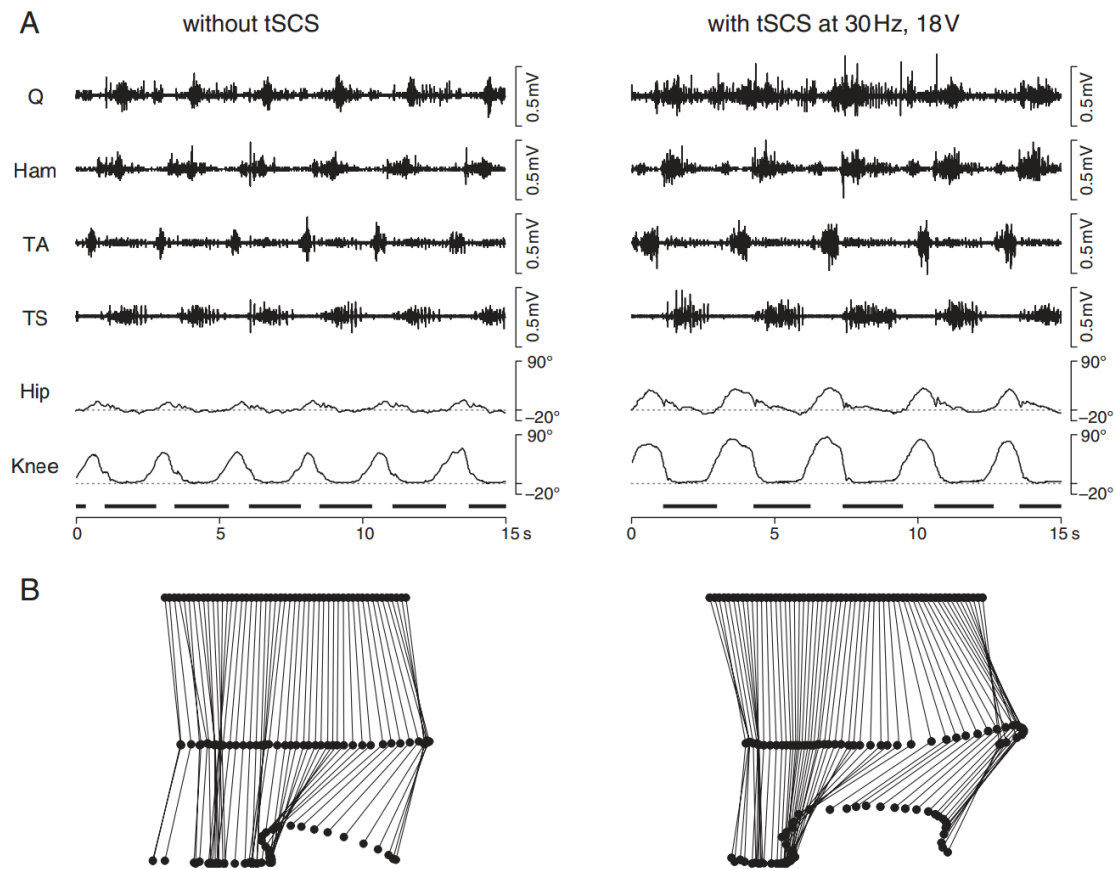


Figure 2.18: This figure shows data gathered from a spinal cord injured individual before and during spinal cord stimulation. Subfigure A shows the electrophysiological data that was recorded with an electromyograph on the quadriceps (Q), hamstrings (Ham), tibialis anterior (TA) and triceps surae (TS) and a goniometer on the hip and knee angles. Subfigure B shows the data calculated from hip and knee angles. The left column shows movement on a treadmill without tSCS and the right column shows the improved gait with tSCS. Source: Minassian et al. (2012)

intensity was chosen in the same way as before. The treadmill was activated again during stimulation. This showed an improvement of the electromyographic activity and in the gait cycle itself. This resulted in a higher foot clearance and stride length which is shown in figure 2.18.

Model

A two-step process was used, therefore two models were calculated in order to get the results. First, a volume conductor model was created, which was solved using Comsol. The output is the electric potential throughout a specific geometry. Paths inside the geometry of the electric potential were used as input to a nerve fiber model. This model is an electrical network model that simulates neurons along a nerve.

3.1 Volume Conductor Model

Electrical stimulation of the spinal cord induces a potential difference between electrodes placed on the back (anode) and an electrode placed on the stomach (cathode). This potential difference creates an ionic current flow through the body, which depends on the shapes and conductivities of the structures in the geometry. To get the resulting potential distribution in the body, a volume conductor model has to be solved, which has specific boundary conditions. The volume conductor problem cannot be solved analytically, therefore the finite element method is used to calculate the steady-state solution.

To solve the problem with the finite element method, the geometry has to be split into smaller parts, finite elements, which are tetrahedrons in this case. The size of these tetrahedrons determines the spatial resolution and therefore the precision of the results. On the contrary, the size also influences memory consumption and speed of the calculation.

A 3D model was created and imported into Comsol Multiphysics, a finite element software

suite. Every part of the geometry was assigned a specific conductivity and the model was meshed by the mesh generator to get a large set of tetrahedrons. This mesh was solved using a stationary solver with the electric currents (DC) module. The way this study was set up was taken from Ladenbauer (2008). Ladenbauer’s master thesis compares 2 different stimulation techniques whereas this study compares different positions of the body. A new and more realistic model was created. The created geometry includes:

- Electrodes
- Skin
- Fat
- General thorax
- Vertebral bone
- Vertebral discs
- Muscle
- CSF
- Vertebral fat
- Spinal cord

Comsol is able to import either a surface or volume model. If a surface model is imported, it is automatically converted in a volume model. The conversion is error-prone, therefore a solid model was created and then imported into Comsol. To get an accurate geometry, 3D image data was used. There are 2 options to use image data: segmented magnetic resonance imaging (MRI) or computer tomography (CT) pictures to get the structures or use already segmented data like the “Virtual Family”. The “Virtual Family” is pre-segmented imaging data that is available in ACIS (Solid) and RAW (Voxel) format. It was created by “Information Technologies in Society” (IT’IS) (Christ et al., 2010).

Computer-aided design (CAD) data can be used without pre-processing, therefore it was imported directly into Comsol. This failed with “The file contains no geometry objects of the requested type”. Several other CAD applications such as Autodesk Autocad, Dassault Systemes Solidworks and Geomagic Geomagic Studio weren’t able to open this cad file. The recommended viewer for the “Virtual Family” is SemCad, which opened the file but didn’t offer any way to edit it, therefore the voxel data was used.

3.1.1 Voxel to surface data

The data was examined with ParaView 3.98.0. An included text file contains important information about the model including the size in voxels ($x=1220$, $y=620$ and $z=3720$), the spacial size (0.0005 m on every axis) and the value of each segmented body part. Some important values can be found in table 3.1.

Table 3.1: Example of segmented parts and their value

Value	Part
13	Cerebrospinal fluid
27	Fat
34	Intervertebral disc
48	Muscle
58	Skin
62	Spinal cord
77	Vertebrae

There is no reliable way to directly convert voxel models into CAD models. Therefore, a surface model was created as an intermediate step, which was then converted into a CAD model. A threshold was applied in ParaView to get only one of the body parts, for example the vertebrae. This yielded an error message that was avoided by creating a subset of the data, containing only the part needed.

An “ExtractSurface” tool was added to remove all inner voxels, which were occluded and therefore were not needed to create a surface model. The result of the tool was exported as comma-separated values (CSV) file, since the height and width of any voxel is not important when creating a surface model by meshing the points. The only relevant thing, the position, was written to a file. The data was imported into Geomagic, but it didn’t show the correct positions.

A Matlab script was written to replace the broken ParaView exporter. All values of the “RAW” voxel format are 8-bit characters consecutively arranged in a specific order of spatial dimensions. The script reads “slices” along the z-axis, searching for the correct character and writes its index into a 3D-array. When it is finished, it is able to find separate structures (like vertebrae) and write them into different files to edit them individually afterwards. It is also able to remove small particles. The size of each structure is determined and if it is smaller than a specified number of voxels it will not be written into the file. The source code of the Matlab script can be seen in listing A.1.

The CSV file is now imported into Geomagic Studio 2012. This application is used to edit 3D scans and create surface and solid models of them. All floating or small fragments were removed by the script, therefore the points can immediately be wrapped (meshed) into a surface. The default settings were used. After wrapping the model contained spikes, holes and wrong face normals. Most of these things were automatically solved by the “MeshDoctor” tool. This tool is able to repair the following issues:

- Non-Manifold Edges
- Self-Intersections
- Highly Creased Edges
- Spikes
- Small Components
- Small Tunnels
- Small Holes

To repair the normals, the segment with incorrect normals was disconnected from all other segments. The normals were flipped and the segment was re-attached. Big holes were filled individually with the “Fill Single” tool, since “Fill All” was sometimes using the wrong curvature which lead to incorrect geometry. The geometry was now correct, resembling the CT or MRI pictures. The segmentation process that is applied to the voxel data is not exact and therefore some geometry looked wrong. For example, some pedicles were too thin or were not connected at all, or the spinal canal was missing on the sacrum. These things were later corrected in the solid model.

3.1.2 Surface to volume data

Solid models in CAD files are mathematical representations of curves that form surfaces. If these surfaces do not form holes, they can be knit into solids. Therefore, the surface model was converted into a solid. There are 2 methods of doing this: each polygon of the model gets converted into a face of a solid. The problem with this method is that the model consists of a large amount of faces and reducing this amount would change the geometry a lot. The second method fits a large surface to lots of small polygons. This needs a longer time for fitting and this process does not always work. Sometimes the faces generated will self-intersect or have bad angles. Before starting the conversion process the geometry had to be smoothed and bumps and groves removed. In most cases it did not work otherwise.

The conversion was started with the “AutoSurface” tool in the “Exact surfaces” tab. The “Geometry Type” was set to “organic”. “Mechanical” failed to convert with this type of geometry. If errors occurred, the conversion was stopped and the problem area was edited before trying again. The finished model was saved as CAD file. The file type was set to .step, since it was the only type that hadn’t shown any problems in Comsol.

After conversion of the vertebral bodies and the skin layer, which acted as general thorax, the models were imported into Comsol. Cubes were inserted as temporary electrodes. The body was subtracted from the cubes to form a surface without overlapping. 0 V were applied to the stomach electrode and 10 V was applied to the back electrode. Meshing did not work with any of the available sizes. Meshing different parts of the model independently didn’t work either. The process of creating the solid model was tweaked by using fewer patches per body and trying to prevent any spikes or deep grooves in any surface. After applying these changes, the model meshed and computed. The model of the vertebra in the different stages of modelling can be seen in figure 3.1.

Now the intervertebral disks and the spinal fat were inserted, which caused meshing to fail again. Since the process of creating the vertebrae had already been optimized, several different versions of the new structures were tested. These versions consisted of voxel and artificially created models with varying amounts of faces and smoothness. The mesher processed for about 1 hour and then showed an error message. With some versions, the meshing did work, but the solver crashed. The most commonly encountered error messages were these:

- Errors while meshing
 - Failed to respect boundary element edge on geometry face.
 - Failed to insert point.
 - Intersecting face elements.
- Errors while computing
 - Undefined value in the stiffness matrix.
 - Failed to evaluate operator.
 - Failed to find a solution.
 - Undefined value found.

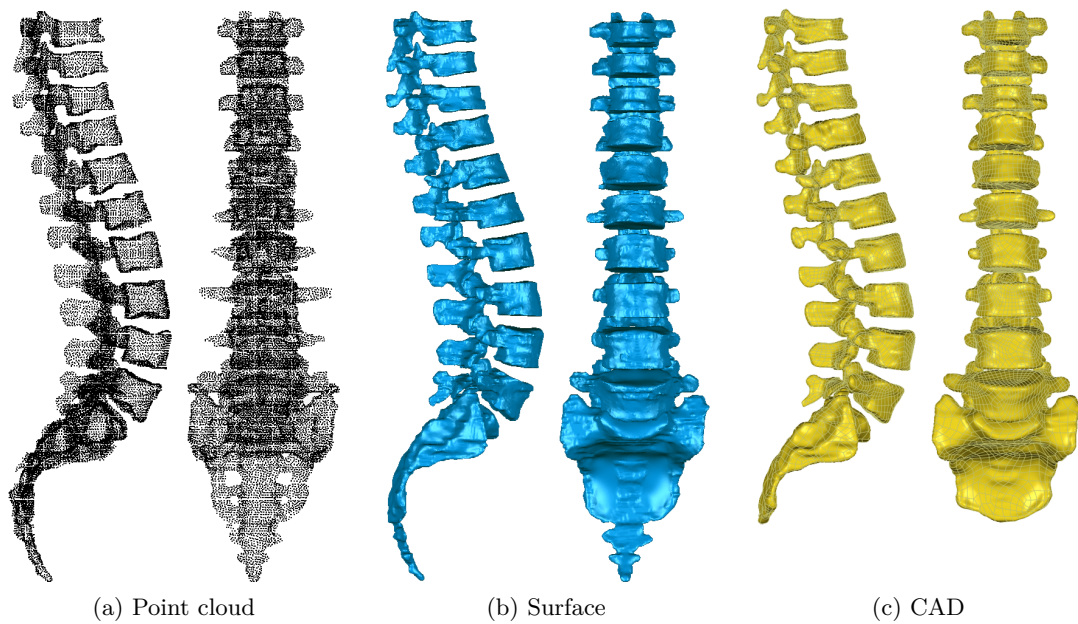


Figure 3.1: The model in different stages of the modelling workflow. These models could not be used in the final simulation because of technical restrictions. In comparison, figure 3.3 shows the workflow that was used for the simulation.

The problem was created by surfaces that were closely together or were overlapping by a small amount. This would cause the mesher to create a great number of very tiny tetrahedrons, which consumed a large amount of memory and caused the mesher to crash. 24 GB system memory and 256 GB virtual memory didn't solve this problem. The geometry had to be completely replaced. To get a working model, surfaces should not overlap at all and should not be too uneven or contain too many faces. This can't be done by using actual scanned data, therefore the solution was to create the model from scratch using Solidworks.

To get the correct sizes, the vertebrae were imported as surface model to get a reference for modeling. The corpus was created by inserting 2 planes, which acted as tangents to the upper and lower surfaces. The outlines of the surfaces were sketched onto these planes. These outlines were connected using the "Lofted Boss/Base" tool. The back of the vertebra was created by using 3 planes, which were perpendicular to the 3 axis. On one of these planes the outline of the reference model was sketched. This sketch was extruded to go completely through the reference. Then the outlines were sketched on the

other 2 planes and everything outside these outlines was cut with the “Extruded Cut” tool. The resulting corpus and back were combined to form a complete vertebra.

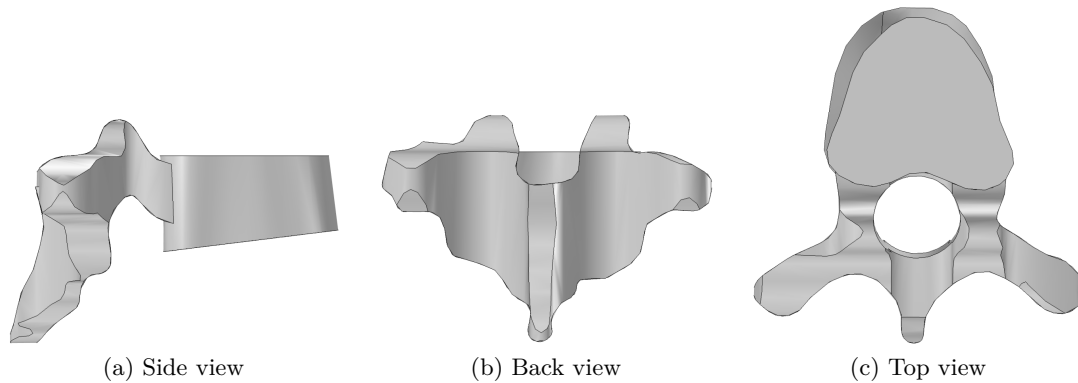


Figure 3.2: The finished CAD model of the Th8 vertebra.

The spinal canal was missing, since it resides inside the outlines. To use realistic sizes, the diameters of the CSF and the vertebral canal were taken from Malinowsky (1911). The size of the vertebral canal varies and was averaged by taking the sum of 3 sizes (previous, current and next) and dividing it by 3. The scaled radii can be seen in table 3.2. The canal was modeled by creating an ellipse with the correct size and then making an extruded cut in a way that the distance between the canal and the front part is minimal. The finished model of a single vertebra can be seen in figure 3.2.

The basic form of the sacrum was built using the same technique as for the vertebrae. The sacral foramina were rebuilt by sketching ellipses on multiple planes. These planes were aligned in a way that all holes were perpendicular to the outside of the sacrum. Since the vertebral canal was also missing from the sacrum, it had to be recreated. Planes were inserted at each vertebral level and ellipses with the correct sizes were sketched on these planes. Just like with the vertebrae before, these ellipses formed the boundaries of bone, fat and CSF. First, the upper side of the sacral canal was created because it was missing from the template. Its thickness was set to 2 mm. It was merged with the other bone structures. The fat was now subtracted from this merged structure and the CSF was subtracted from the fat. The intervertebral foramina were represented by subtracting cones from the bone at the exit point of the root fibers. These cones were small on the exit points but grew bigger further away.

A body was created by creating a plane above the spine and sketching a 40 cm by 20 cm area. This area was extruded with the “Swept Boss/Base” tool in the same shape as the

spine. This was done by creating a second sketch, which acts as the extrude path. To get electrodes with the correct thickness, the outline was sketched and this sketch was projected onto the surface of the body. The projection was then extruded to the desired thickness. The spine, body and electrodes were imported into Comsol and meshed. It was now discovered, that the mesher somehow doesn't work correctly with round surfaces, since the electrodes wouldn't mesh. The circle in the electrode sketch was then replaced by a polygon, which meshed correctly.

When the number of objects was observed, it was discovered that there was a large amount of objects, but there should have been 14 at this stage. By hiding the 14 biggest objects, many small parts were discovered. These fragments were a result of overlapping bodies, because when Comsol finalizes the geometry each overlapping part becomes a part itself. This had to be corrected since small parts can cause the mesher to crash. To fix this, the overlapping parts were either cut from the involved bodies or moved to prevent overlapping. Now everything meshed and computed fine.

3.1.3 Post processing

The intervertebral discs were created by connecting the upper and lower surfaces of 2 corpora with the "Lofted Boss/Base" tool. The fat was created by inserting a cylinder the same size the cut of the vertebral canal was made. It is important that this does not intersect with any vertebrae or intervertebral discs. Any intersection will cause either additional geometry or "Intersecting edges" errors during meshing. The fat has to be longer on the lower part. This will be cut at the upper plane of the next corpus, to ensure all parts are touching. If they do not touch, they cannot be connected to one entity. The CSF is created the same way as the fat. Drawing an ellipse, extruding it downward and cutting it at the upper plane of the next body.

The spinal cord was created in a different way. Spinal cord sizes were taken from Kameyama et al. (1996), which are measured at each spinal cord segment. These sizes were taken from Japanese men. To get values that would apply to a middle-age caucasian man, the width had to be scaled so that the thickest part measures 1 cm. The scaled sizes can be seen in table 3.2. A plane was inserted at all vertebral levels. Segments that correspond to only one specific vertebral body are connected immediately. All other segments are connected when the vertebral bodies are combined into one single file. This ensures that the spinal cord will follow the rotation of the bodies. The same was done with fat and CSF whose dimensions can be found in table 3.3. The muscles

were also created per body. This has to be done because it has to be ensured that each body, including their additional structures, are completely inside the muscle. Some tests were made with partly encased bodies, but it failed to mesh because of geometry errors. Another option would be to leave a certain distance between muscles and bodies. This option is very difficult to do because it has to be very exact and can't overlap anywhere. The individual muscle parts are later connected to a single object.

Table 3.2: Radius of the spinal cord in [mm] at different spinal cord levels. Source: Kameyama et al. (1996)

Spinal cord level	Spinal cord radius scaled	
	Sagittal	Transverse
TH8	2.87	4.25
TH9	2.87	4.25
TH10	2.93	4.37
TH11	2.93	4.31
TH12	2.99	4.43
L1	3.05	4.48
L2	3.22	4.60
L3	3.56	4.89
L4	3.68	5.00
L5	3.56	4.77
S1	3.22	4.25
S2	2.70	3.68
S3	2.30	2.99

Another problem specific to Solidworks was encountered, but it was difficult to fix, because it meant that everything had to be created from scratch. This problem was size restrictions. There are basically 2 kinds of restrictions in Solidworks. There can be no coordinate bigger than 500 or smaller than -500 on any axis. This limits the size of the body, because its top plane has the coordinate $z=500$. Objects cannot be copied if they are larger than 500. Solidworks will simply output “the object is too large”. Copying is very important, because if a subtraction between two object has to be created, the source objects will be gone. Therefore, they have to be copied beforehand and the copies can be used for subtraction. Also, the body created is 500 on the z-axis. To get it higher, an extrusion has to be made in Comsol. Scaling is also not possible because it has the same limitations as copying.

Now the other 2 models were created. To get the spine to lean to the front and to the back all vertebral bodies had to be rotated. It was decided that each single rotation

Table 3.3: Radii of fat and CSF inside the vertebral canal in [mm]. Source: Malinowsky (1911)

Vertebral level	CSF average radius		Fat average radius	
	Sagittal	Transverse	Sagittal	Transverse
TH8	5.67	7.50	8.50	10.67
TH9	5.33	7.67	8.67	10.50
TH10	5.17	7.33	9.00	10.83
TH11	5.50	7.17	9.33	10.50
TH12	5.67	7.50	9.33	11.17
L1	6.00	8.33	8.00	10.67
L2	6.00	9.50	8.50	11.33
L3	5.83	9.00	9.00	12.33
L4	5.83	8.50	10.83	15.17
L5	5.50	6.67	8.67	17.00
S1	4.00	4.50	6.33	19.17
S2	2.33	2.50	4.00	15.50
S3	1.00	1.25	2.33	9.67
S4			2.00	4.25

will be 3° . The rotation itself was done by using the “Move/Copy” tool. First L5-T8 + internal structures were selected and rotated. The origin of the rotation was set according to Schmidt et al. (2008). Next, the same was done with L4-T8, L3-T8, etc. When all rotations were completed the curvature of the body and the position of the electrodes had to be changed. At last, the models had to be checked again for intersections between elements, because some were created by the rotation. Since spinal cord, fat, CSF and the muscles consisted of multiple slices they had to be combined into single objects before importing them into Comsol.

3.1.4 Comsol

A new model was started in Comsol. The space dimension was set to 3D, the physics was set to ‘Electric Currents (ec)’ and the study type was set to “Stationary”. The finished model was imported into Comsol. It usually showed a warning “Could not respect relative repair tolerance.” but this was ignored, because it worked fine. First, the model was finalized, this is done automatically if anything below “Finalize Geometry” is selected. The element count showed 2 more elements than Solidworks because the fat and dura are cut where the muscle ends. This cannot be avoided. The material had to be set for

every structure. The list of conductivity was set according to Ladenbauer (2008). These values can be seen in table 3.4.

Table 3.4: Values of conductivity of different structures. The values of the “standard” column were chosen. This table is taken from Ladenbauer (2008). The extreme values in the columns “Min” and “Max” are from Foster and Schwan (1989); Gabriel et al. (1996); Geddes and Baker (1967); Gu et al. (2002); Kuhn (2008); Miklavčič et al. (2006); Raicu et al. (2000).

Structure	Conductivity [Sv m^{-1}]			References
	Min	Standard	Max	
Electrode inter-face	0.0001	0.01	1	Overall impedance measurements
Skin	0.0001	0.0025	0.003	
Fat	0.002	0.04	0.1	(Malmivuo, 1995; Geddes and Baker, 1967)
General thorax	0.2	0.25	0.3	(Coburn, 1985; Geddes and Baker, 1967; Rattay et al., 2000; Szava, 2006)
Muscle (transversal)	0.04	0.08	0.17	(Malmivuo, 1995; Foster and Schwan, 1989)
Muscle (longitudinal)	0.2	0.5	0.8	
Vertebral bone	0.01	0.02	0.03	(Szava, 2006)
Intervertebral disc	0.47	0.6	0.65	(Gu et al., 2002; Szava, 2006)
Epidural fat	0.002	0.04	0.1	(Struijk et al., 1991, 1992, 1993a)
CSF	1.5	1.7	1.7	(Rattay et al., 2000; Holsheimer, 1998a)
Grey matter	0.17	0.23	0.23	(Struijk et al., 1991, 1992, 1993a)

Special attention had to be given to the muscle conductivity, since it is the first of 2 structures with anisotropic conductivity. Simple axis based anisotropy could not be used, because the conductivity would be wrong in most cases. The conductivity had to adapt depending on the position. This was done by rotating the conductivity vector C around the x-axis. A polynomial $f(z)$ was created, which follows the path of the muscles on the yz plane. The conductivity depends on the direction of each position, so the derivative of the polynomial $f'(z)$ was calculated. The angle of rotation ψ was computed by calculating the angle between the z-axis and the derivative at this point. Now, the new conductivity vector C_n was calculated by multiplying the rotation matrix R_x with the conductivity vector C . C_n was entered as vector in the material settings in Comsol. C_x , C_y and C_z was substituted by the values found in table 3.4.

$$z = \begin{pmatrix} 0 \\ 0 \\ 1 \end{pmatrix}, V = \begin{pmatrix} x \\ f(z) \\ z \end{pmatrix}, V' = \begin{pmatrix} 0 \\ f'(z) \\ 1 \end{pmatrix}, C = \begin{pmatrix} C_x \\ C_y \\ C_z \end{pmatrix} \quad (3.1)$$

$$\cos(\psi) = \frac{z * V'}{|z| * |V'|} = \frac{1}{\sqrt{f'(z)^2 + 1}} \Rightarrow \psi = \arccos \frac{1}{\sqrt{f'(z)^2 + 1}} \quad (3.2)$$

$$R_x = \begin{pmatrix} 1 & 0 & 0 \\ 0 & \cos -\psi & -\sin -\psi \\ 0 & \sin -\psi & \cos -\psi \end{pmatrix}, C_n = R_x * C = \begin{pmatrix} C_x \\ C_y \cos(-\psi) - C_z \sin(-\psi) \\ C_y \sin(-\psi) + C_z \cos(-\psi) \end{pmatrix} \quad (3.3)$$

The conductivity for the white matter works in the same way as the conductivity of the muscles, but with different values for C_x , C_y and C_z . After all conductivities had been set, the skin and fat conductivities were adjusted so that the total body resistance of the neutral model results in 700Ω . The resistance was calculated by measuring the current on the zx-plane and using Ohm's law. After lowering the conductivity for the skin to $0.00108 \text{ Sv m}^{-1}$ and for the fat to 0.02 Sv m^{-1} the resistance was 695.41Ω . With the same conductivities, the resistance of the forward leaning model was 699.79Ω and the resistance of the backward leaning model was 638.16Ω . The voltages of the electrode surfaces had to be set to induce a potential difference. An "Electric potential" element was inserted under "Electric currents (ec)". The voltage of the stomach electrode was set to 0 V and the voltage of the back electrodes was set to 10 V . The outer surface of the electrodes were selected and added to the boundary selection. Now the model was meshed with the element size set to "Finer". The model in different stages including the result of the mesher can be seen in figure 3.3. All finished models of the 3 body positions can be seen in figure 3.4. The study was now computed. The statistics of the simulations can be seen in table 3.5.

Table 3.5: Simulation statistics for all 3 simulations done on a Intel i7 930 Quad-core processor with 24GB DDR3 RAM.

Position	LinIt	LinErr	LinRes	Time	DOF	Elements	Boundary elements
Neutral	59	0.00095	4.6e-007	227s	5032910	3555787	694045
Front	59	0.00074	3.7e-007	236s	5125825	3618884	711624
Back	59	0.001	5.1e-007	234s	5271408	3721545	733756

The ratio of current normal to the CSF to the total current going through the body was measured after the simulation. This could not be done directly in Comsol since Comsol is

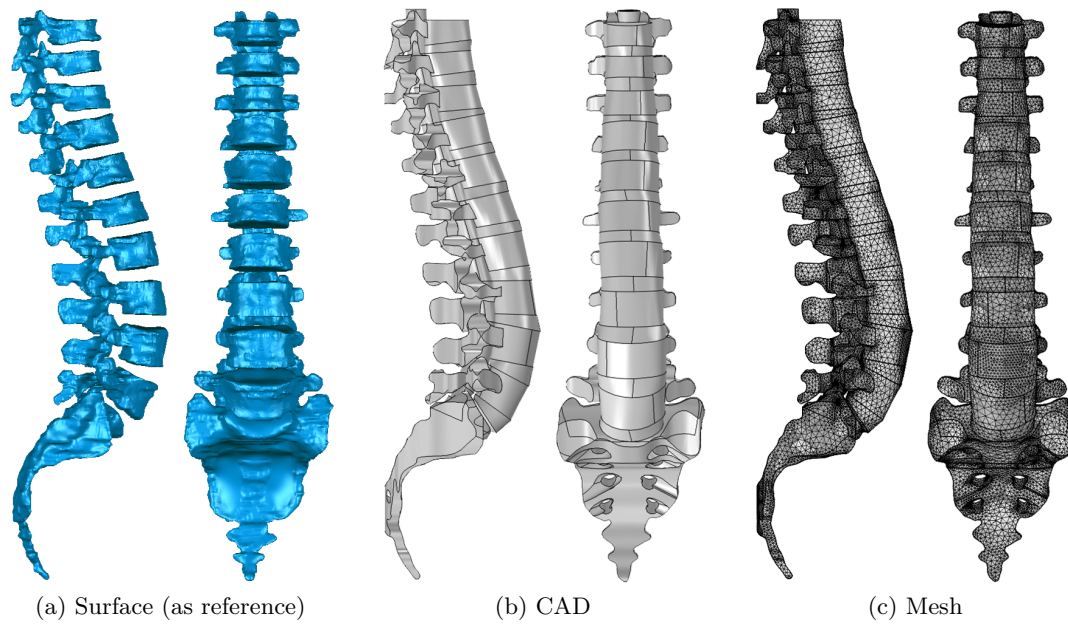


Figure 3.3: The model in different stages of the modelling workflow. In comparison figure 3.1 shows the old workflow, which couldn't be used for simulation.

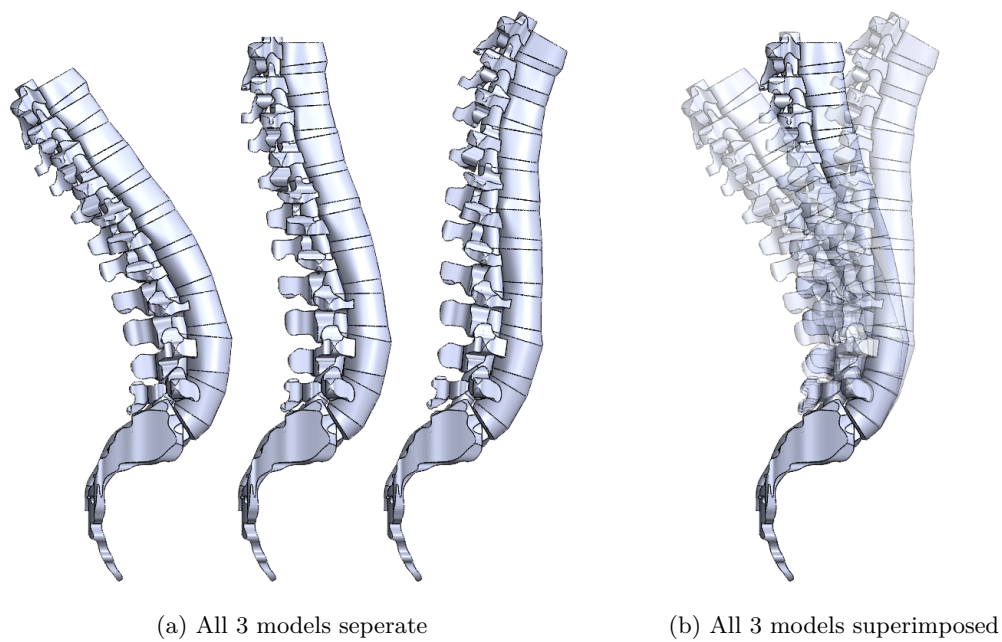


Figure 3.4: The finished models. Left: Leaning backward, Middle: Neutral, Right: Leaning forward.

not able to calculate the current normal to a surface. Therefore, Matlab in combination with the Comsol plugin was used. The script in listing A.2 was used for this task. It shows the total current by calculating the current through the electrodes (Surfaces 58 and 626) and it gets the current through the CSF by calculating the current through all surfaces of the CSF domains (33 and 36) and dividing it by 2 because the current is counted twice: when entering the CSF and when leaving it.

3.2 Nerve Fiber Model

To analyze the voltage along the nerve root, the paths of the root fibers were marked in the solid model. This had to be done for spinal levels L1 to S2, both left and right + anterior and posterior for all 3 models, which resulted in 84 root fibers. To get the most accurate result, points along the fiber path were marked at each vertebral level. The T11-L2 points were taken according to Wall et al. (1990) and the L2-S2 points were taken from Cohen et al. (1991). These points served as template to draw the paths along them. The starting points of every fiber were marked using the mapping from vertebral to spinal levels from Minassian (2000), which analyzes data from Lang and Geisel (1983) and Lang (1984). Every sketch contains one nerve path, which consists of several lines and splines. All sketches were exported as separate CSV files with a visual basic for applications (VBA) script, which can be seen in listing A.3.

A Matlab script was used to do a cubic interpolation between these points and plot all points to verify that they are correct. This had to be done because the exported sketches didn't have enough points to get a smooth diagram. The interpolation was used to get a maximum distance of 0.1 mm between each point. The script can be seen in listing A.4 and the resulting paths can be seen in figure 3.5.

All points are exported into one text file for Comsol, another text file is created with information on how to split the file again. The list of points is used in Comsol to evaluate the electric potential. The resulting file is then split afterwards to get individual files for the simulation of the root fiber excitation. The resulting files each contain the extracellular potential along the outside of one nerve fiber. The electrical network model of McIntyre et al. (2002) can now be used to calculate what happens inside these nerve fibers. A graphical representation of the model can be seen in figure 3.6.

The model is a double cable model, where the myelin sheath and the nerve fiber are separate conductors. The geometrical and electrical parameters were determined by

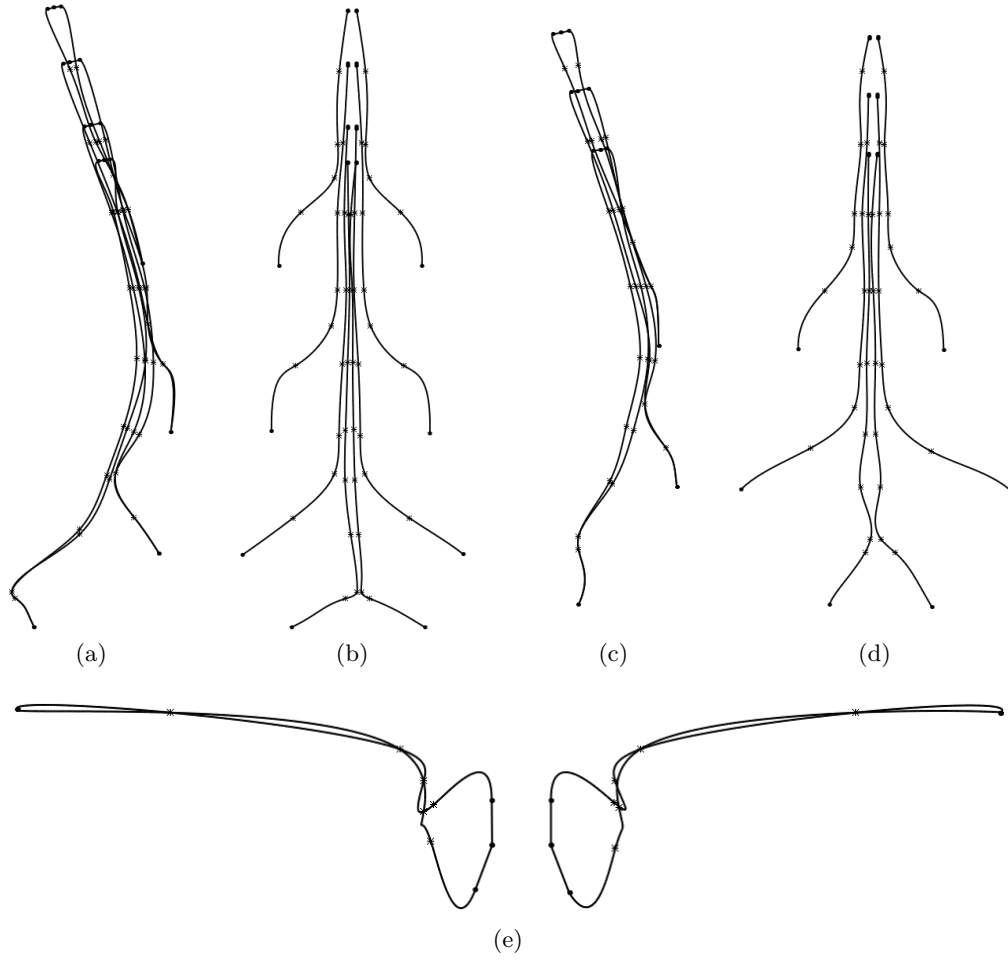


Figure 3.5: Nerve roots at different levels in different views. Figure (a) and (b) show the root nerves for vertebral levels L1, L3, L5 and S2 while figure (c) and (d) show the nerves for L2, L4 and S1. (a) and (c) show the sagittal view, (b) and (d) show the frontal view. All these figures only show one side because the other side would be nearly covered. This means the right half is hidden in the sagittal view and the anterior half is hidden in the frontal view. Figure (e) shows all root nerves of vertebral level L1.

experimental measurements on humans, cats and rats. The model divides the nerve fibers into nodal and non-nodal parts which alternate. The nodal segment is the node of Ranvier, the non-nodal segments are internodal segments (STIN), paranodal main segments (FLUT) and paranodal myelin attachment segments (MYSA). Subfigure b of figure 3.6 shows the electrical network of the model. Table 3.6 shows the geometric parameters and 3.7 shows the electrical parameters which the model uses.

Table 3.6: Geometric parameters used for simulation of the nerve fiber model. Source: McIntyre et al. (2002)

Description	Value
Fiber diameter	16 μm
Node-node separation	1500 μm
Number of myelin lamella	150
Node length	1 μm
Node diameter	5.5 μm
MYSA length	3 μm
MYSA diameter	5.5 μm
MYSA periaxonal space width	0.002 μm
FLUT length	60 μm
FLUT diameter	12.7 μm
FLUT periaxonal space width	0.004 μm
STIN length	228.8 μm
STIN diameter	12.7 μm
STIN periaxonal space width	0.004 μm

Table 3.7: Electrical parameters used for simulation of the nerve fiber model. Source: McIntyre et al. (2002)

Param.	Description	Value
c_n	Nodal capacitance	2 $\mu\text{F cm}^{-2}$
c_i	Internodal capacitance	2 $\mu\text{F cm}^{-2}$
c_m	Myelin capacitance	0.1 $\mu\text{F cm}^{-2}$
ρ_a	Axoplasmic resistivity	70 $\Omega \text{ cm}$
ρ_p	Periaxonal resistivity	70 $\Omega \text{ cm}$
g_m	Myelin conductance	0.001 S cm^{-2}
g_a	MYSA conductance	0.001 S cm^{-2}
g_f	FLUT conductance	0.0001 S cm^{-2}
g_i	STIN conductance	0.0001 S cm^{-2}
g_{Naf}	Maximum fast Na^+ conductance	3 S cm^{-2}
g_{Ks}	Maximum slow K^+ conductance	0.08 S cm^{-2}
g_{Nap}	Maximum persistent Na^+ conductance	0.01 S cm^{-2}
g_{Lk}	Nodal leakage conductance	0.007 S cm^{-2}
E_{Na}	Na^+ Nernst potential	50 mV
E_K	K^+ Nernst potential	-90 mV
E_{Lk}	Leakage reversal potential	-90 mV
V_{Rest}	Rest potential	-80 mV

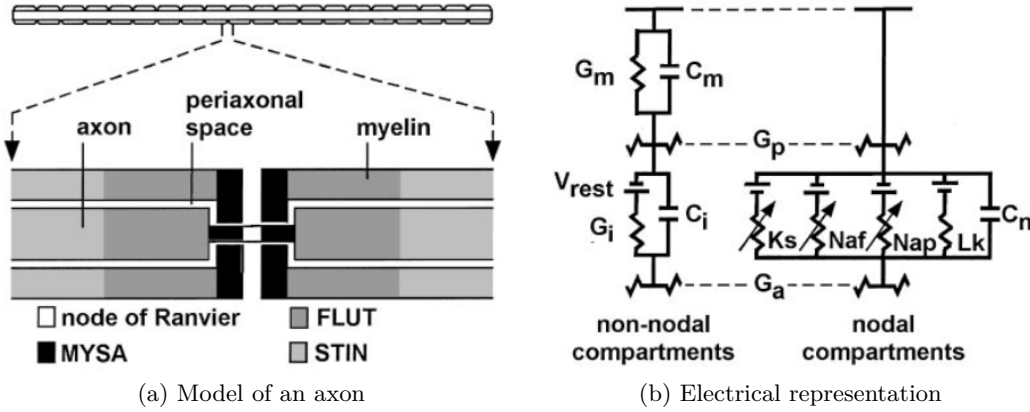


Figure 3.6: Subfigure a shows the geometric representation of the nerve fiber model. It is divided in 4 different regions: internodal segment (STIN), paranodal main segment (FLUT), paranodal myelin attachment segment (MYSA) and node of Ranvier. The dimensions of these structures can be found in table 3.6. Subfigure b shows the electrical representation of nodal and non-nodal compartments. The electrical parameters can be found in table 3.7. Source: McIntyre et al. (2002)

All non-nodal segments consist of 2 parts: The myelin sheath, which is represented by the myelin capacitance (c_m) and conductance (g_m) in parallel, and the nerve fiber, which is represented by the internodal capacitance (c_i) in parallel to rest potential (V_{Rest}) and conductance (g_a , g_f or g_i). The nodal segment consists of a parallel combination of fast Na^+ conductance (g_{Naf}), slow K^+ conductance (g_{Ks}), persistent Na^+ conductance (g_{Nap}) and nodal leakage conductance (g_{Lk}) with their respective potentials and the nodal capacitance (c_n).

A stimulus with 1 ms pulse duration, 16 μm fiber diameter and cathodic stimulation is simulated with various voltages. To get the excitation threshold the script will start with -1 V and do a binary search until the threshold is found.

Results

Section 4.1 of this chapter shows the results of the volume conductor model, which are electric potentials and current densities throughout the model. Section 4.2 contains the results of the nerve fiber model which is calculated using the data of the volume conductor model. It shows the excitation thresholds of different root fibers and the positions where these excitations are evoked. It also shows the source of this data, which are extracellular voltage profiles and the corresponding second-order derivatives.

4.1 Results from the Volume Conductor Model

The ratio of the current through the CSF to the total current emitted from the electrodes was determined. The neutral position shows the best ratio with 5.74%, leaning forward shows the second best with 5.53% and leaning backward the worst with 5.17%. The ratio of the current through the spinal cord to the total current was also determined. Leaning forward showed the best ratio with 0.97%, leaning backward has 0.93% and upright has 0.72%. This big difference between the upright model and the other 2 models doesn't reflect in the thresholds, which is shown in figure 4.6.

Figure 4.1 displays a cut along the centerline of the model where the electric potential and current density can be seen. The overall potential is lower when leaning backward (subfigure (c)) while the current density through the spinal cord is the highest. This is also evident in figure 4.4. The current density spreads up and down when leaning forward

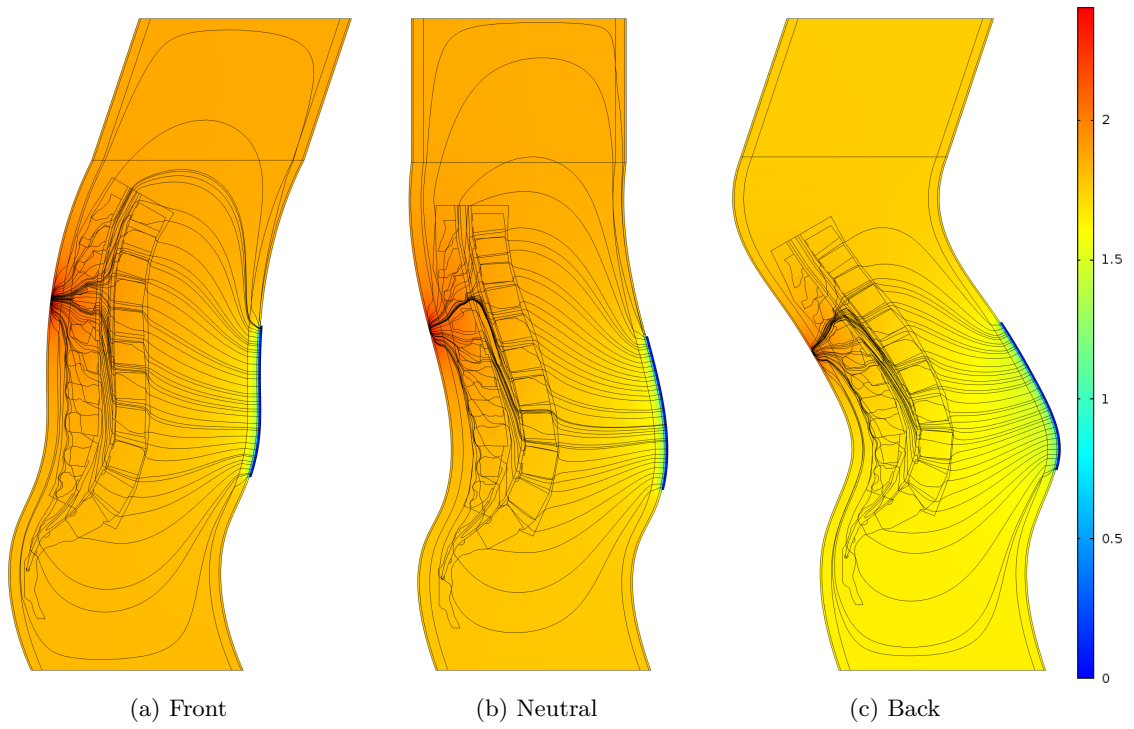


Figure 4.1: Cut through the saggital plane in the center of model. Streamlines show the current density and the colors display the electric potential in [V].

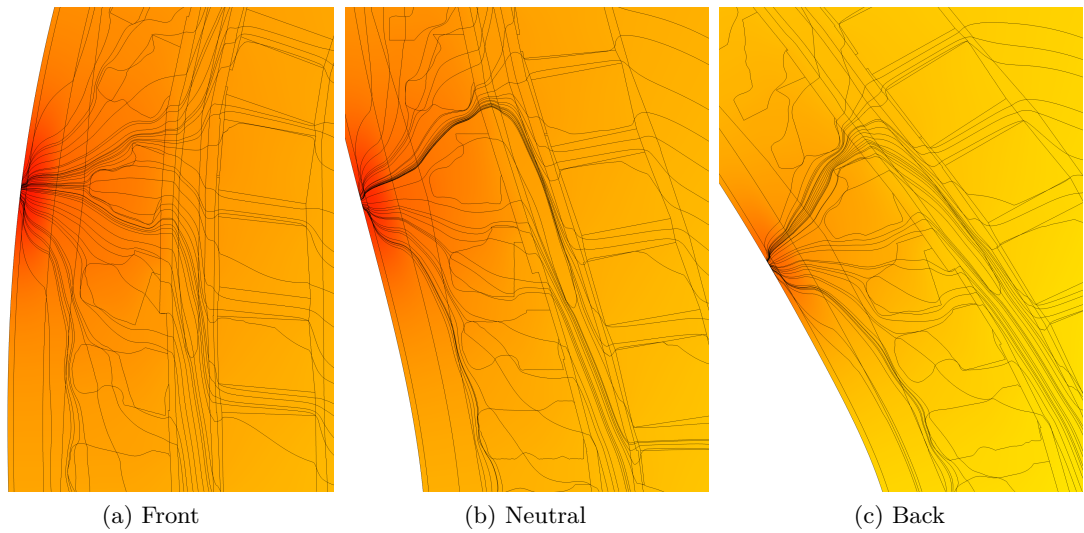


Figure 4.2: Same as figure 4.1, but zoomed in, showing the point of the highest current density and the terminal spinal cord.

(subfigure (a)) while there is a downward focus in the upright position (subfigure (b)) and when leaning backward.

To get a better look on the most important area, figure 4.2 contains the same subfigures as 4.1 but zoomed in on the point of the highest current density and the terminal spinal cord. It shows in more detail that the high current density area is between Th10 and Th11, and between Th11 and Th12 when leaning forward and only between Th10 and Th11 in the other 2 positions. This is the result of too low positioned back electrodes in the forward leaning model, which was later confirmed by figure 4.5.

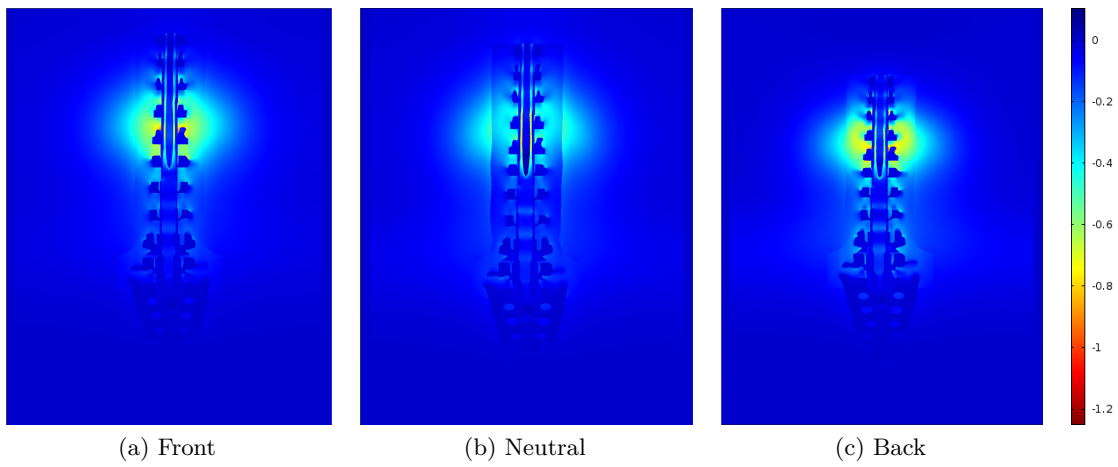


Figure 4.3: Cut along the vertebral canal shows the current density in $[A/m^2]$ normal to the spinal cord.

The current density normal to the spinal cord is shown in figure 4.3. All 3 positions show a high current density area, which is on the level of the electrodes and excludes the vertebrae and the spinal cord. This area is more intense when leaning forward or backward. The maximum intensity is on the top edge of the Th12 vertebra for all positions. It is located inside the vertebral canal for the upright position and outside the canal in the other 2 cases. The effect of the intervertebral discs can be seen in the vertebral canal below the spinal cord. The current density inside the muscles is higher when leaning backward which can be seen on the shine around the vertebrae.

The upper plot of figure 4.4 shows the electric potential in the CSF posterior of the spinal cord. Leaning backwards shows a lower overall potential because the resistance of the model is generally lower. This is described in section 3.1.4. Moving the electrode

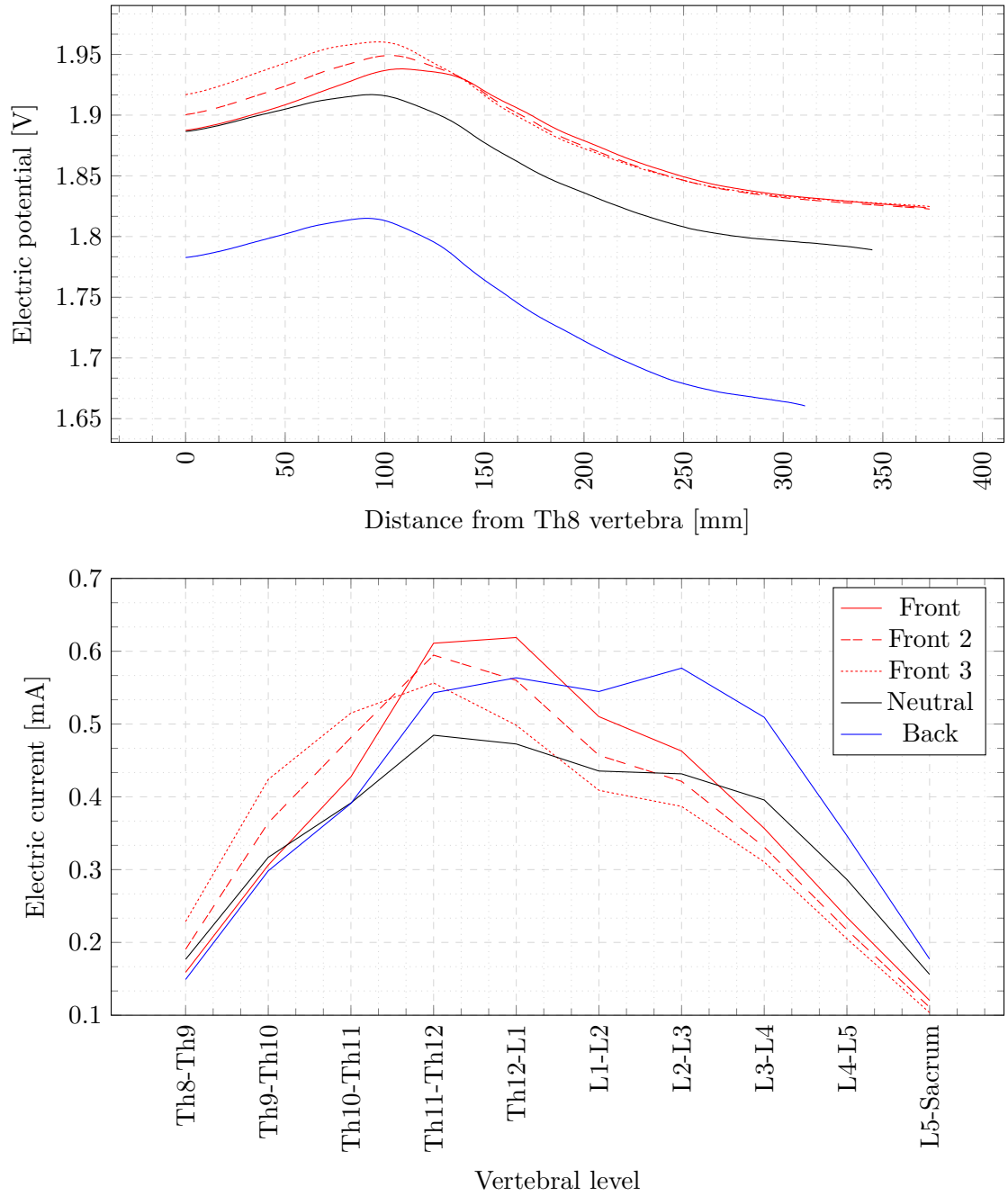


Figure 4.4: The upper plot shows the potential distribution measured along an imaginary fiber which traverses the CSF laterally centered posterior of the spinal cord from Th8 to the sacrum. The lower plot shows the current through the intervertebral discs. “Front 2” and “Front 3” show a modified version of the forward leaning model (“Front”) were the back electrodes were moved crannially by 15 mm and 30 mm respectively.

upwards in the forward leaning model from 0 mm to about 140 mm results in a higher potential.

The lower plot of figure 4.4 shows the current through each individual intervertebral disc. While the backward and neutral position show nearly consistent values in 4 discs from Th11-Th12 to L2-L3, leaning forward has a peak in 2 discs: Th11-Th12 and Th12-L1. This is not as pronounced when the back electrodes are moved cranially: While these two discs still have the highest values, the peak at Th11-Th12 is higher. Additionally, while the potential increases when the electrode is moved upwards, the overall current through the discs decreases.

When comparing figure 4.4 and 4.6 it is evident that even though leaning backwards has the lowest potential in the CSF and a lower current through the intervertebral discs than leaning forward, it has the lowest thresholds of all models on the lower root fibers. This means that the threshold is not directly influenced by the potential or the current, but probably by the current density. Figure 4.5 shows the current density longitudinal and transversal to an imaginary fiber in the CSF positioned posterior of the spinal cord.

The position of the electrodes is evident in the longitudinal plot where the current density starts to increase. When looking at the original 3 simulations (“Front”, “Neutral”, “Back”) it is apparent that the electrodes of the forward leaning model are placed too low, because the current density starts to rise later than in the other 2 models. To determine a better position for the electrodes two additional models were created: one where the back electrodes were moved cranially by 15 mm and one where they were moved by 30 mm from their initial position. Both of these simulations show an improved current density, which can be seen in “Front 2” and “Front 3”.

Overall the backward leaning model shows the best results longitudinally and the forward leaning model transversally. The peaks in the transversal plot are because of the intervertebral discs, which are more conductive than the vertebrae. Therefore, the transversal current can only pass at the intervertebral discs, while the longitudinal current is only mildly affected by the presence of the discs.

4.2 Results from the Nerve Fiber Model

Figure 4.6 shows the excitation thresholds for all 3 positions separated by nerve root type (Anterior, Posterior, Left, Right). The highest thresholds belong to the first forward

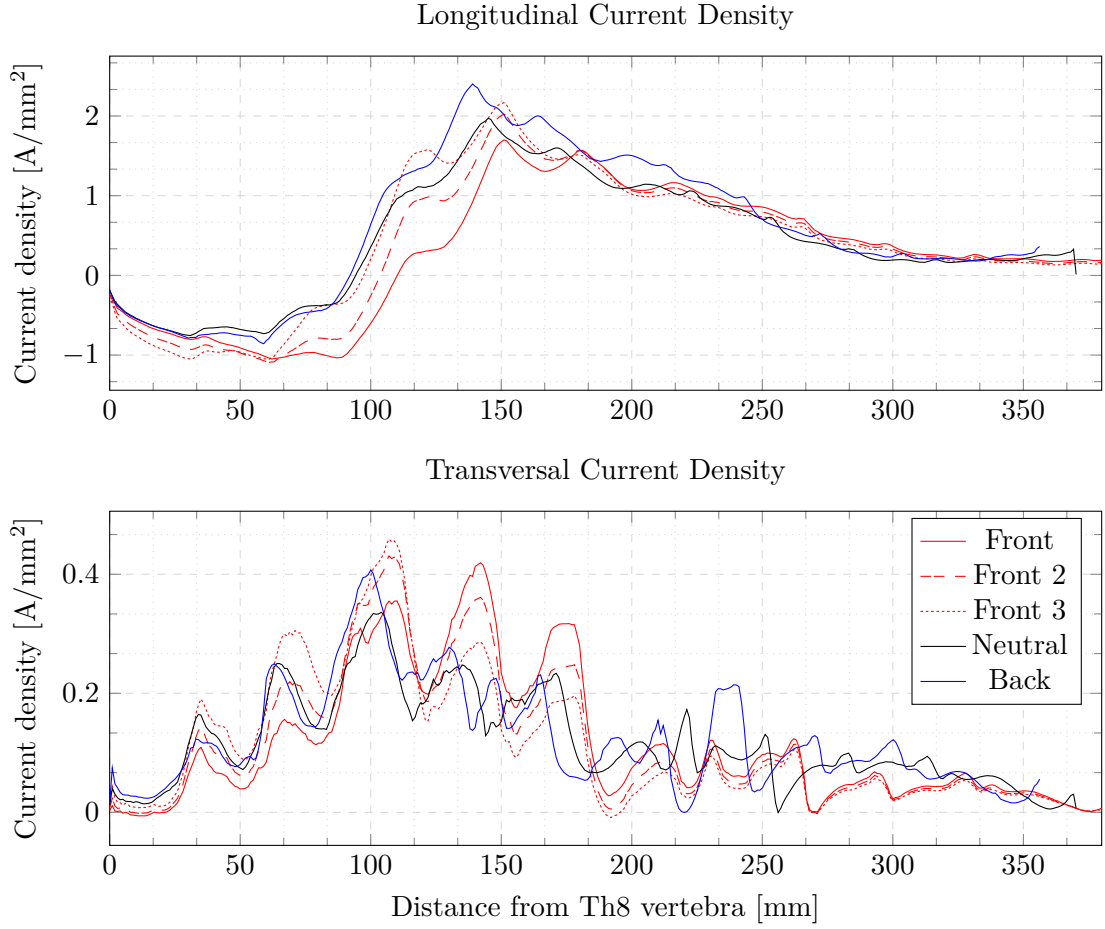


Figure 4.5: Logitudinal and transversal current density measured along an imaginary fiber which traverses the CSF laterally centered posterior of the spinal cord from Th8 to the sacrum. “Front 2” and “Front 3” show a modified version of the forward leaning model (“Front”) were the back electrodes were moved crannially by 15 mm and 30 mm respectively.

leaning model in most cases. The largest differences between leaning forward and backward regarding thresholds are at vertebral levels L5-S2 on the anterior fibers and L1-L3 on the posterior fibers. When comparing leaning backward and neutral there seems to be nearly no difference in the posterior fibers and only slight differences in the anterior fibers. Moving the back electrodes cranially lowers the thresholds significantly in the posterior roots, but they are still higher than in the other 2 models in most cases. The lowest thresholds of the posterior fibers belong to the forward leaning model for L1-L2 and to the backward leaning model for L3-S2. On the anterior fibers the thresholds

decrease on levels L1-L4 and increase on L5-S2. Subfigure 5 and 6 show the ratio between anterior and posterior thresholds. It is nearly constant for “Front 2”, “Neutral” and “Back”. “Front” has unusually high thresholds on the upper posterior roots and therefore a low ratio. “Front 3” has the highest thresholds of all models on the anterior roots and the lowest of the upper posterior roots and therefore a very high ratio.

Figure 4.7 shows data similar to figure 4.6 except that every fiber was cut into 2 parts between the upper and lower peak of the second-order spatial derivative. The upper half of the fibers has a higher threshold on anterior root fibers, while the lower half has a higher threshold on posterior root fibers. The shape of figure 4.6 seems to mostly depend on the low threshold parts, which are the lower part of the anterior roots and the upper part of the posterior roots. Interestingly the ratio for all lower parts is about 1 which means that thresholds are the same for the anterior and posterior roots.

Figure 4.8 shows the excitation thresholds of the neutral position with centered spinal cord from figure 4.6 and the thresholds of the same model with the spinal cord moved ventral by about 5 mm. It is evident that moving the spinal cord has a negligible effect on the thresholds.

Figure 4.9 shows all excitation positions. There are no differences between positions in the posterior fibers. All excitation positions lie directly after the exit point where the fibers leave the spinal cord. L2-S2 of the anterior fibers have the same excitation positions for all body positions. These are the exit points of the spinal canal for L2-S1 and the point where the fibers leave the spinal cord for S2. Only S1 shows differences between the different positions.

Figure 4.10 and figure 4.11 show the data that was used to get excitation positions of figure 4.9 and the excitation thresholds of figure 4.6. Figure 4.10 shows the left anterior fibers and figure 4.11 the left posterior fibers. Since left and right root fibers yield nearly the same results, the results of the right side can be found in the appendix. The first column shows the extracellular voltage which was extracted from the simulated model along the fiber paths. The other 3 columns show the second-order derivative of these voltage profiles. This second-order derivative is proportional to the activating function (see equation 2.10).

A big peak in the derivative will not always lead to an excitation. This is evident when viewing the results of the posterior fibers. In the simulation, the excitation took place

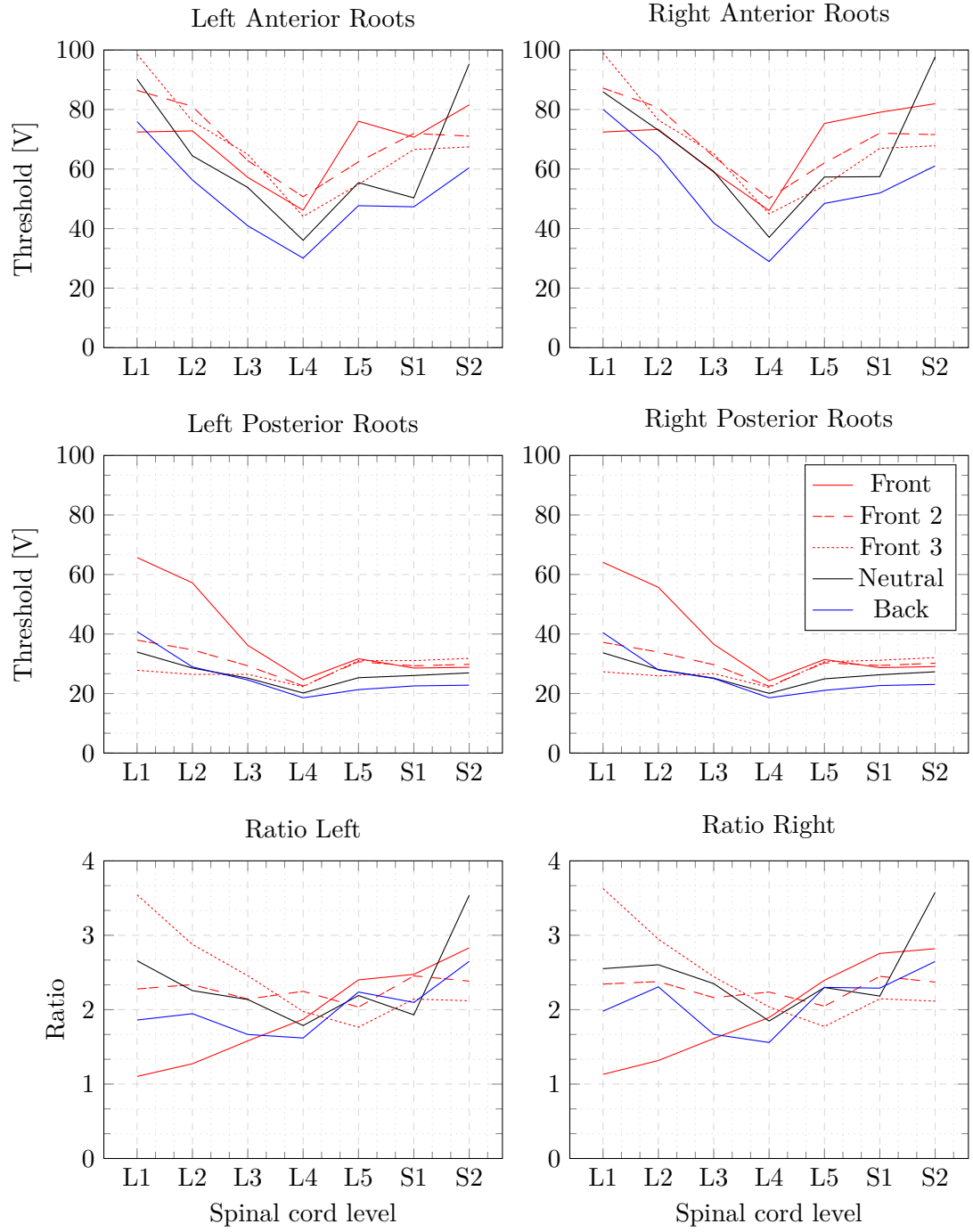


Figure 4.6: This figure shows the excitation thresholds to evoke action potentials in different root fibers. “Front 2” and “Front 3” show a modified version of the forward leaning model (“Front”) were the back electrodes were moved crannially by 15 mm and 30 mm respectively. The anterior thresholds are divided by the posterior thresholds in subfigure 5 and 6 to show if the ratio changes with each respective spinal cord level.

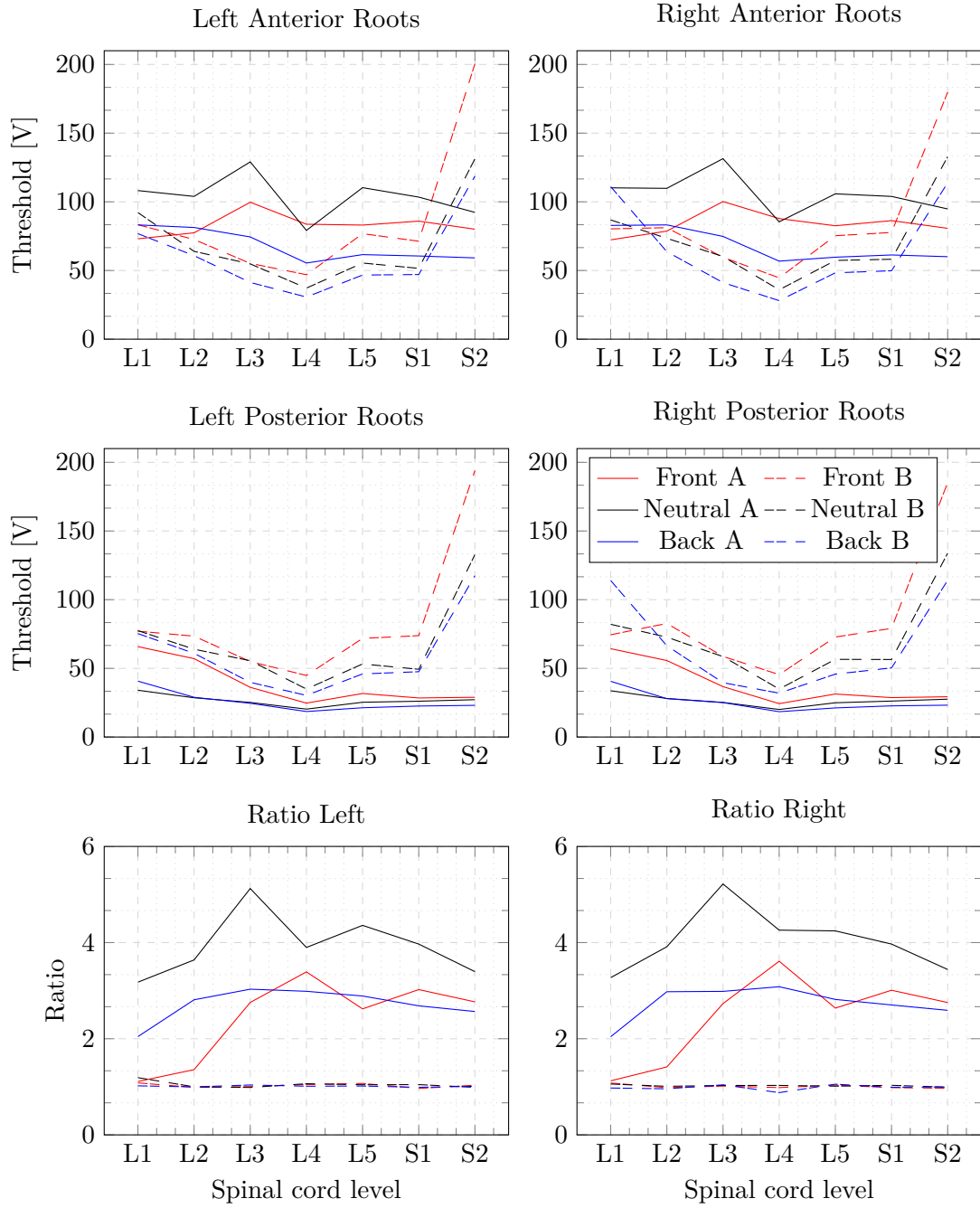


Figure 4.7: This figure shows the excitation thresholds to evoke action potentials in different root fibers. The path of each fiber was cut between the upper and lower peak of the second-order derivative of figure 4.10, 4.11, A.1 and A.2. The resulting two parts were used as input for the nerve fiber model. The solid curves belong to the upper part of the fiber while the dashed curves belong to the lower part. The anterior thresholds are divided by the posterior thresholds in subfigure 5 and 6 to show if the ratio changes with each respective spinal cord level.

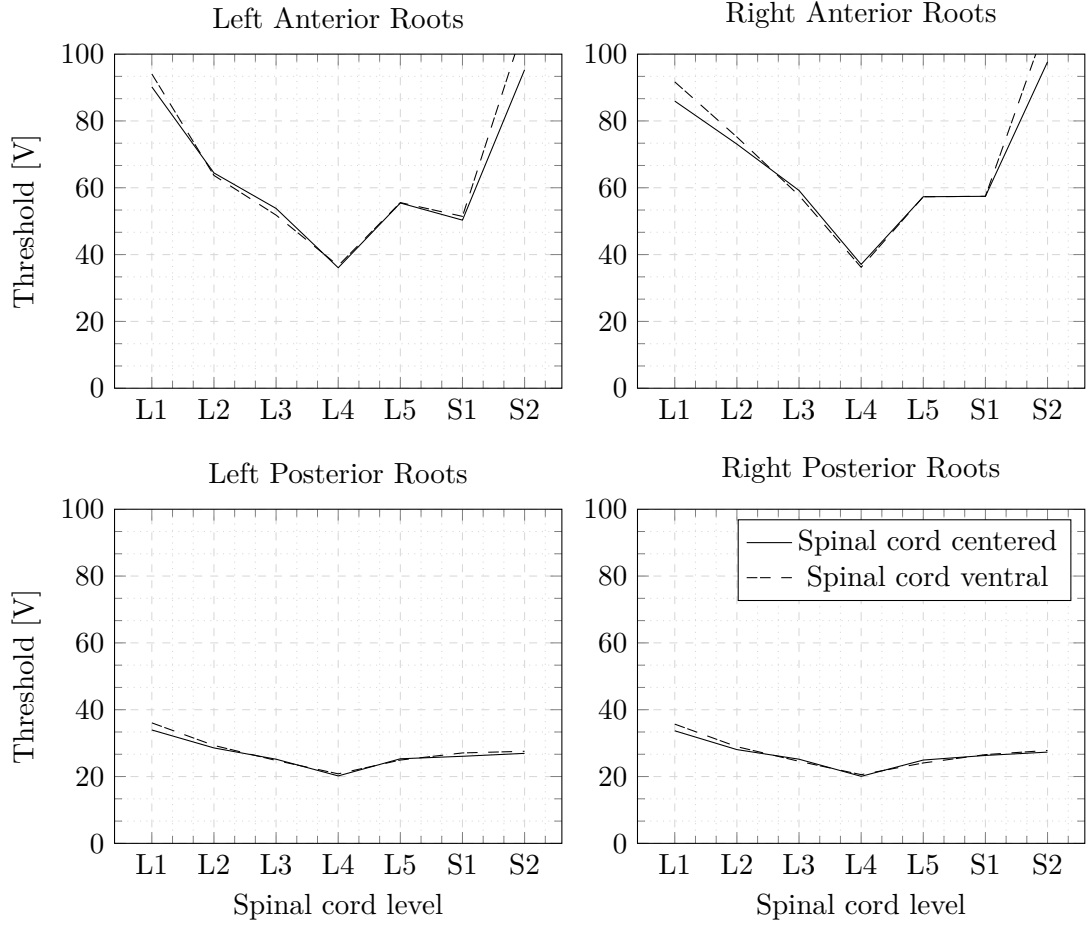


Figure 4.8: This figure shows the excitation thresholds to evoke action potentials in different root fibers in [V]. The solid line shows the thresholds of the upright model with the spinal cord centered (same as 4.6) and the dotted line with the spinal cord moved ventral.

when the fiber left the spinal cord, but sometimes the lower peak (when the fibers leave the spinal canal) is larger. This happens because the sum of adjacent peaks is important. Therefore, if a peak is followed by an equally large negative peak, they will cancel each other out and no excitation will occur.

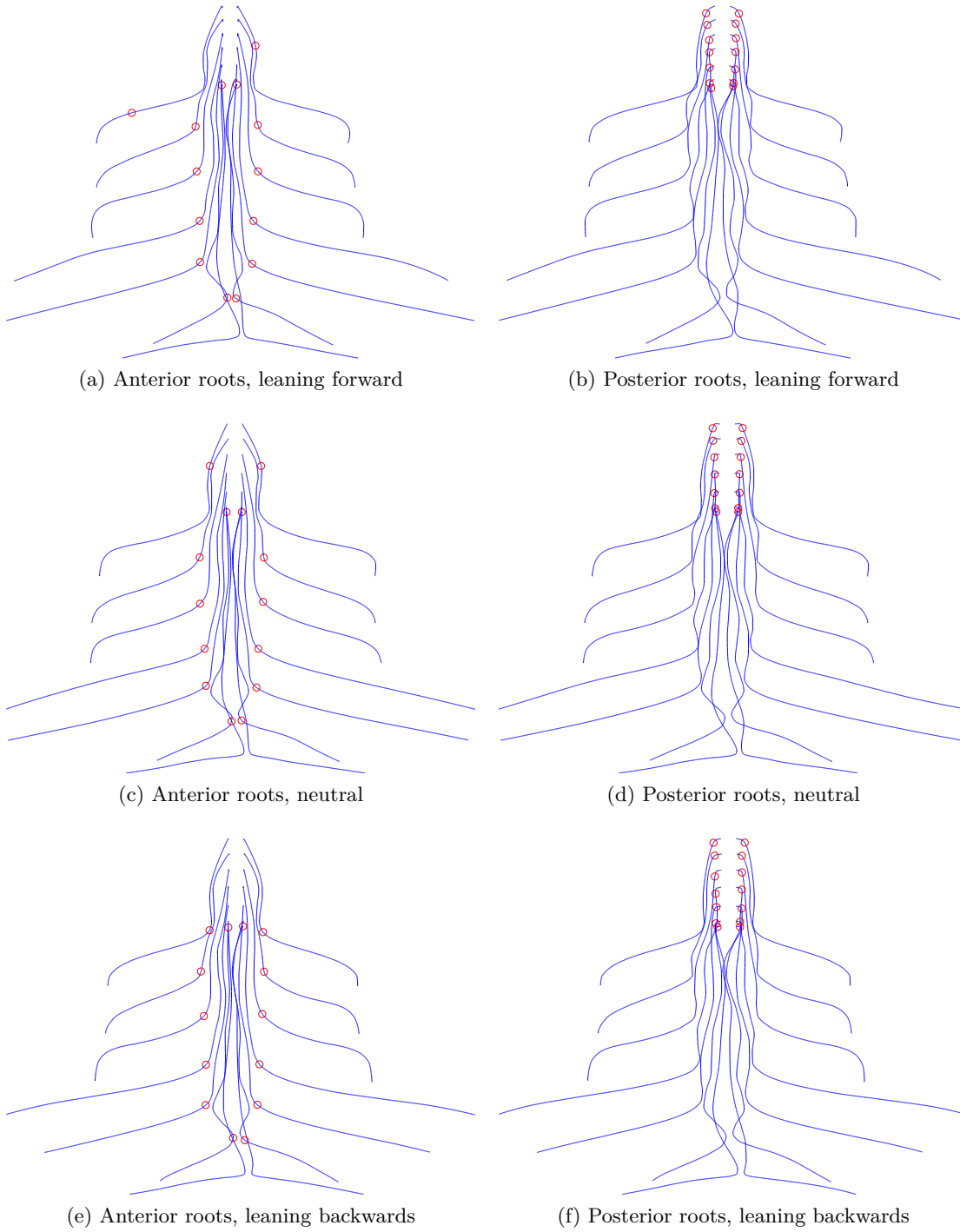
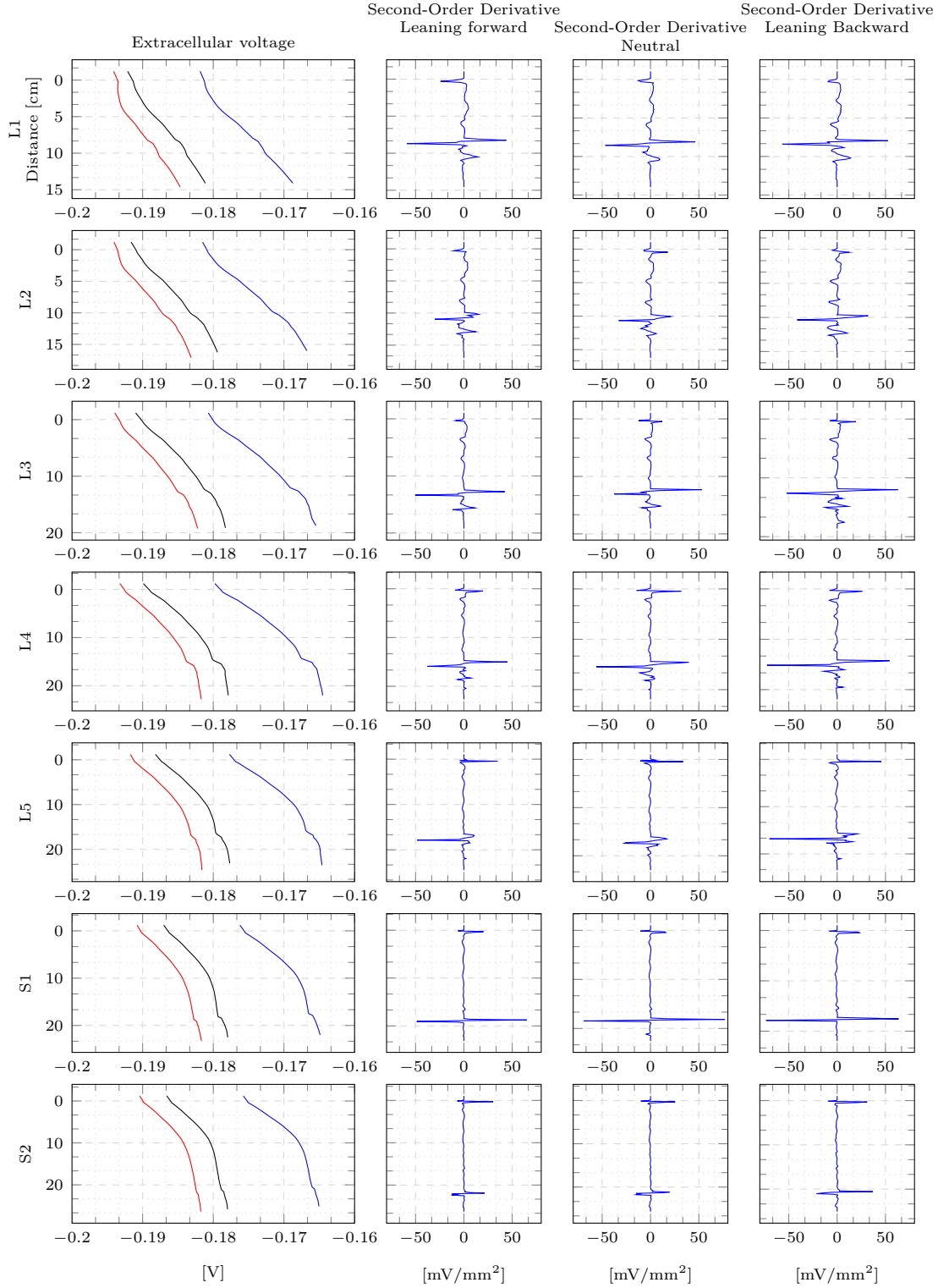


Figure 4.9: This figure shows the positions of the action potential evocation on anterior and posterior roots in different stances.



58 Figure 4.10: Extracellular voltage and its second-order derivative of the left anterior roots in different positions. Colors of the curves in the extracellular voltage diagram indicate the position: **leaning forward**, upright, **leaning backward**.

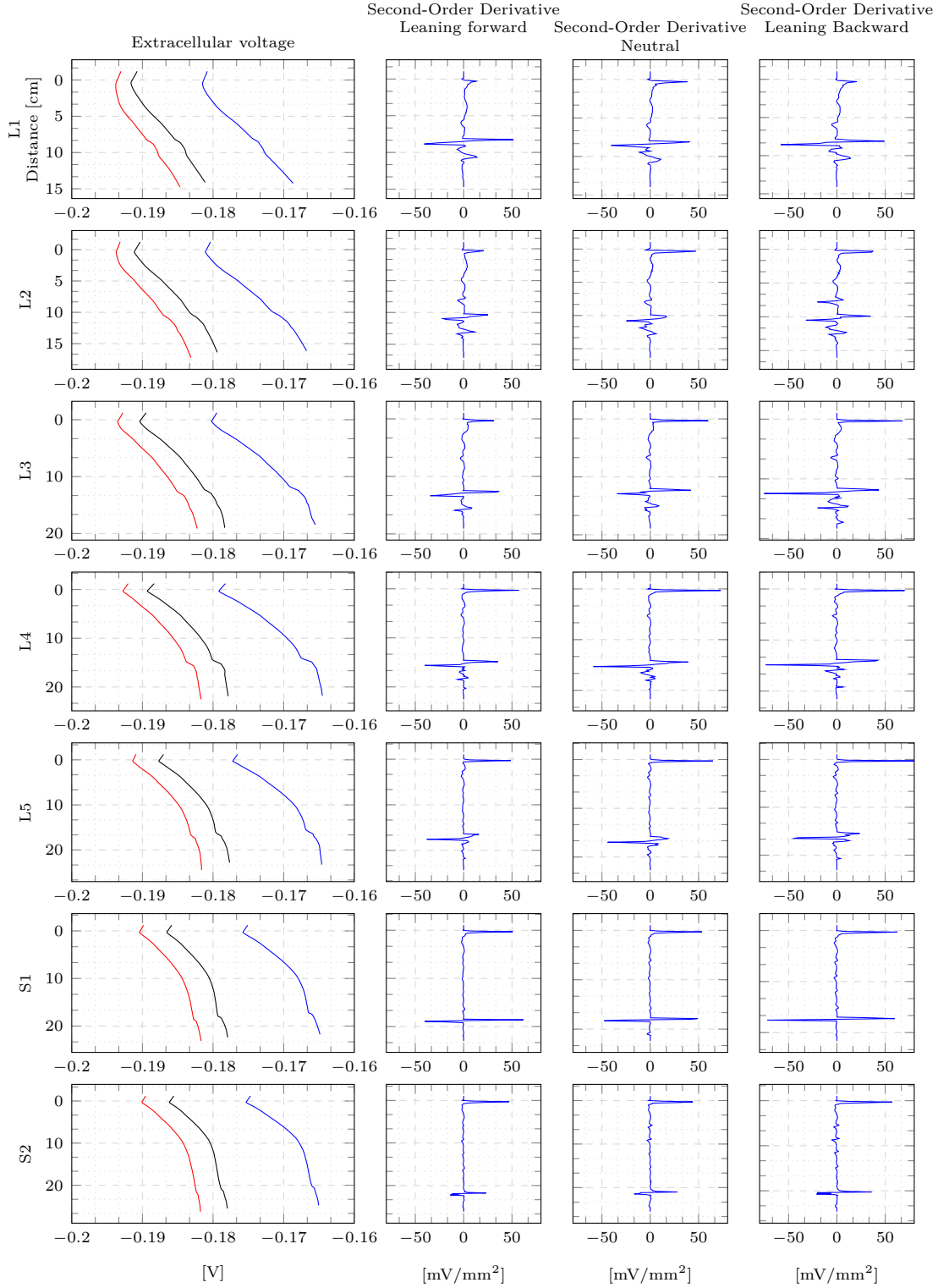
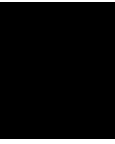


Figure 4.11: Extracellular voltage and its second-order derivative of the left posterior roots in different positions. Colors of the curves in the extracellular voltage diagram indicate the position: **leaning forward**, upright, **leaning backward**.



Discussion

The results show that the thresholds for the excitation of the posterior root fibers are not directly connected to the electric potential in the CSF or the current through the intervertebral discs. Leaning backwards shows the lowest absolute electric potential, but has the best results regarding thresholds. The same is true for the neutral position of the spine: It shows the lowest current through the CSF but has thresholds which are nearly as good as leaning backward.

The first version of the forward leaning model showed larger absolute values of the electric potential and current, but had the highest thresholds of all models. The reason for this behavior was found when examining the current densities along and transversally to the spinal canal of these models: For all models there is a point, approximately at the level of the electrode, where the current density along the spinal canal is 0. At this point current densities, and hence the electric field, are exclusively oriented orthogonally to the spinal canal. Below this point the longitudinal component is directed caudally and above rostrally. In the leaning forward-model this zero-crossing-point of the longitudinal current density is shifted by a few centimeters in caudal direction. These observations suggested that placing the electrodes at a more rostral location would counter some of the observed effects on the activation thresholds. To confirm this observation 2 additional models were created with the back electrodes moved cranially by 15 mm and 30 mm, respectively. Both models show a higher overall potential and a lower current through the intervertebral discs. Their results are a big improvement on the first version, but the model with the electrodes moved by 30 mm outperforms the 15 mm model. Activation

thresholds of L1 to L4 innervating posterior roots were decreased to a level comparable to the leaning backwards and neutral models. Thresholds of posterior roots of L5 and below were slightly increased. The slope on the current density matches with the other 2 positions and the thresholds are closer than before and in some cases better than in the other models.

Leaning backward has the lowest thresholds from L3 to S2 and leaning forward in L1 and L2. The thresholds of the neutral position lie between the thresholds of the other 2 positions. When the root fibers were simulated as 2 parts divided between the 2 hot spots it became evident that the posterior roots favor the upper part of the roots, where they leave the spinal cord, and the anterior roots favor the lower part. This is also supported when observing the excitation positions of the single part root fiber simulation: While the posterior roots are generally excited at the entry point of the spinal cord, most of the anterior roots are excited where the fibers leave the spinal canal. Moving the spinal cord from the center to the edge of the vertebral canal has only a negligible effect on the thresholds of the root fibers.

Compared to Danner et al. (2011, 2014) my model shows threshold voltages in the same range. The activating function (Rattay, 1999) shows the same 2 hot spots and locations of action potential initiation as Danner et al. (2014) and Ladenbauer (2008). One of these 2 spots forms where the nerve root fiber leaves the spinal cord, due to the high curvature at the beginning and the medium change from the spinal cord to the CSF. The second spot forms when the nerve root fiber leaves the spinal canal, due to the medium change from CSF to general thorax. Due to these similarities it can be assumed that my model adequately captures the properties of transcutaneous spinal cord stimulation, described by the previous models.

Holsheimer et al. (1995) has shown that the position of the spinal cord in the vertebral canal has a great influence on the effectivity of epidural SCS. Since the spinal cord moves when the position is changed (Holsheimer et al., 1994; Ranger et al., 2008), this may also be true for tSCS. Shifting the spinal cord in the spinal canal almost did not affect the thresholds of posterior- and anterior root activation in this model of transcutaneous stimulation. It is likely that epidural stimulation is influenced by entirely other factors. For example the electric field that is generated by bipolar epidural electrodes is generally much smaller than the field generated by tSCS and spinal nerves are not located between the two electrodes but rather beside them. This means that small distance changes have a much larger effect in epidural stimulation. If the spinal cord shifts only a few millimeters,

the results change vastly. This on the other hand has a negligible effect when using tSCS, because the spinal cord (and its nerves) lie between the two electrodes. This also has one major disadvantage: Since the current must pass through different structures on the way from electrode to electrode, these structures influence the path of the current which affects the excitation threshold.

This means on the other hand that geometric changes of all structures, such as switching body position, have an effect on the thresholds. This is also supported by the results. Leaning forward showed the highest thresholds from L3 to S2, while leaning backwards has the lowest thresholds on the same range. Only L1 and L2 show lower thresholds when leaning forward and replacing the electrodes. The reasons for this are the aforementioned hot spots, maxima in the second order spatial derivative of the potential along the fibers. The peaks in this derivative are smaller when leaning forward, which results in a higher threshold.

This can also be explained using the geometry of the root fibers and the current density. The root fibers consist geometrically of 2 parts: They leave the spinal cord nearly horizontally and continue nearly vertically after a sharp bend. This means the current density can act on the fibers in 2 ways: longitudinally and transversally. Since the posterior root fibers are always activated at the point where they enter the spinal cord and their threshold is determined by the second order spatial derivative of the electric potential along the nerve fiber we can split the processes that create this low threshold site into two components: the first derivative of the potential, i.e. the electric field, from the entry point into the spinal cord and from the entry point in caudal direction along the spinal canal. Their sum corresponds to the second order spatial difference of the potential, i.e., the activating function. Thus, the longitudinal and the transversal components of the electric field at the point where the fiber enters the spinal cord both influence the thresholds of the fibers. The transversal component lowers the posterior and increases the anterior root fiber thresholds (when the back electrode is a cathode). The longitudinal component in caudal direction lowers and in rostral direction increases the thresholds for both fiber classes. When a strong transversal electric field component is present, a point of hyperpolarization is created at the exit of the anterior root from the spinal cord. If, at locations caudal to the electrode level, the transversal component vanishes and the longitudinal component is relatively increased, an activation hot spot with cathodic stimulation is also created at the exit of the anterior roots from the spinal canal.

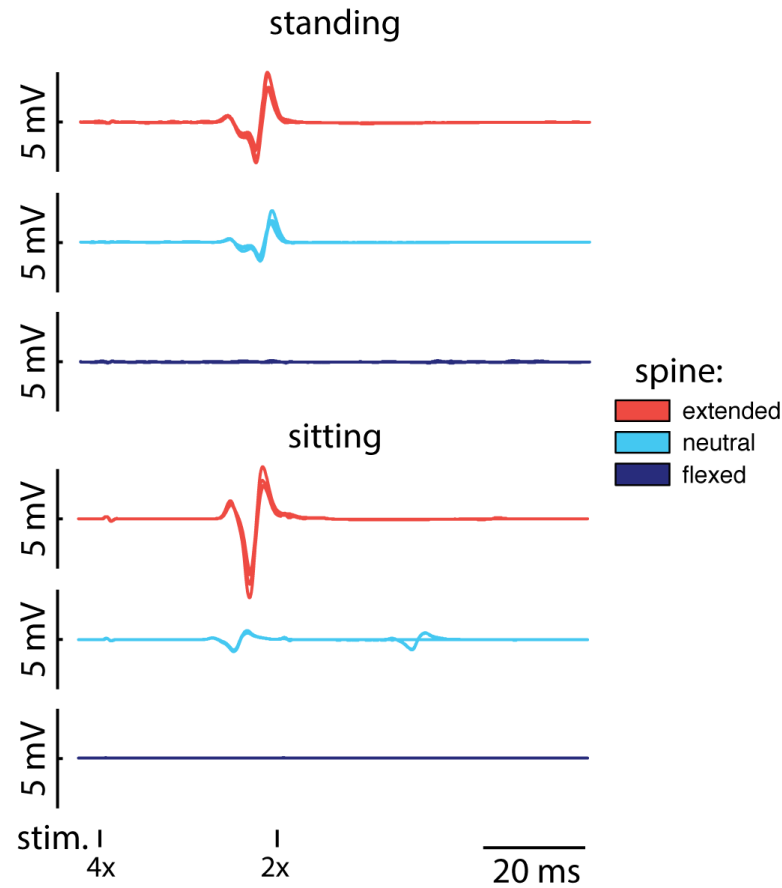


Figure 5.1: Measured data while standing and sitting with 3 different spinal curvatures. This figure shows that afferent stimulation happened when the spine was extended while standing and sitting, or when the spine curvature was neutral while standing. Efferent stimulation happened while sitting with neutral curvature. A flexed curvature resulted in no stimulation. This means that extended curvature is advisable when doing tSCS.

It is possible to explain the preference for the lower hot spot of the anterior roots the same way with the potential distribution. The excitation is likely to happen when the potential difference is high. When considering the posterior fibers the potential decreases from the bend to the spinal cord and it also decreases from the bend downward. This results in a high overall potential difference at the bend. In the anterior fibers on the other hand the potential decreases from the spinal cord to the bend, which means the bend has a low potential from the spinal cord and a high potential downward which cancel each other out and result in a low overall potential difference at the bend.

In general, for neuromodulation purposes, afferent fiber stimulation is desired (Holsheimer,

1998b). This means that the stimulation should provide input to the target circuits in the central nervous system and not simply activate muscles. Most sensory fibers (afferents) are contained within the posterior roots. When applying two consecutive stimulation pulses within a short interval, we can observe the effects of post-activation depression. In case of predominant stimulation of motor fibers the second response will be of equal size than the first, yet if mostly sensory fibers were stimulated a suppression of the second relative to the first response will be observed. This allows us to judge whether the observed responses were predominantly caused by direct activation of sensory or motor fibers. One important factor that influences if the stimulation is afferent or efferent is the position of the body. The results show that this will be the case if an upright or backward body position is used. Figure 5.1 shows preliminary data of measurements, which also support this hypothesis. In the presented model, the ratio between posterior and anterior root stimulation is significantly lowered in the upper lumbar segments, which innervate the quadriceps, when the spine is bent in forward direction. Similar observations were made experimentally.

Following the results of this thesis it may be advantageous to use an upright or backward body position when using tSCS. Since people with an injured spinal cord tend to unintentionally flex when sitting, it may be better to stimulate while lying on the back or even while standing to ensure an upright vertebral column.

Bibliography

- Anatomy Body Gallery. Spinal Cord. URL <http://anatomybodygallery.com/spinal-cord-structure/1770/spinal-cord-5>. Last visited on 22.11.2014. (Cited on page 8)
- C. A. Angeli, V. R. Edgerton, Y. P. Gerasimenko, and S. J. Harkema. Altering spinal cord excitability enables voluntary movements after chronic complete paralysis in humans. *Brain: A Journal of Neurology*, 137(Pt 5):1394–1409, May 2014. (Cited on page 1)
- E. A. Blair and J. Erlanger. A comparison of the characteristics of axons through their individual electrical responses. *American Journal of Physiology – Legacy Content*, 106(3):524–564, 1933. (Cited on page 22)
- Blausen Medical. Multipolar Neuron. URL <http://blausen.com/?Topic=9495>. Last visited on 22.11.2014. (Cited on page 13)
- T. Cameron and K. M. Alo. Effects of posture on stimulation parameters in spinal cord stimulation. *Neuromodulation: Journal of the International Neuromodulation Society*, 1(4):177–183, Oct. 1998. (Cited on page 2)
- K. X. Charand. Action Potentials. URL <http://hyperphysics.phy-astr.gsu.edu/hbase/biology/actpot.html>. Last visited on 04.10.2014. (Cited on page 15)
- S. Y. Chiu, J. M. Ritchie, R. B. Rogart, and D. Stagg. A quantitative description of membrane currents in rabbit myelinated nerve. *The Journal of Physiology*, 292:149–166, July 1979. (Cited on page 19)
- A. Christ, W. Kainz, E. G. Hahn, K. Honegger, M. Zefferer, E. Neufeld, W. Rascher, R. Janka, W. Bautz, J. Chen, B. Kiefer, P. Schmitt, H.-P. Hollenbach, J. Shen, M. Oberle, D. Szczerba, A. Kam, J. W. Guag, and N. Kuster. The Virtual Family—development of surface-based anatomical models of two adults and two children for dosimetric simulations. *Physics in Medicine and Biology*, 55(2):N23–N38, Jan. 2010. (Cited on page 30)
- B. Coburn. A theoretical study of epidural electrical stimulation of the spinal cord - Part II: Effects on long myelinated fibers. *IEEE Transactions on Biomedical Engineering*, BME-32(11):978–986, Nov. 1985. (Cited on page 39)

- B. Coburn. Neural modeling in electrical stimulation. *Critical Reviews in Biomedical Engineering*, 17(2):133–178, 1989. (Cited on page 18)
- M. S. Cohen, E. J. Wall, C. W. Kerber, J. J. Abitbol, and S. R. Garfin. The anatomy of the cauda equina on CT scans and MRI. *The Journal of bone and joint surgery. British volume*, 73(3):381–384, May 1991. (Cited on pages 10 and 42)
- S. M. Danner, U. S. Hofstoetter, J. Ladenbauer, F. Rattay, and K. Minassian. Can the human lumbar posterior columns be stimulated by transcutaneous spinal cord stimulation? A modeling study. *Artificial organs*, 35(3):257–262, Mar. 2011. (Cited on pages 2, 23, 24 and 62)
- S. M. Danner, U. S. Hofstoetter, and K. Minassian. Finite element models of transcutaneous spinal cord stimulation. In *Encyclopedia of Computational Neuroscience*. Springer Verlag, 2014. ISBN 9781461466741. (Cited on pages 23 and 62)
- M. R. Dimitrijevic, M. M. Dimitrijevic, H. Kern, K. Minassian, and F. Rattay. Electrophysiological characteristics of H-reflexes elicited by percutaneous stimulation of the cauda equina. In *Program No. 411.17. 2004 Neuroscience Meeting Planner*, San Diego, CA, 2004. (Cited on page 24)
- R. L. Drake. *Gray’s anatomy for students*. Churchill Livingstone/Elsevier, Philadelphia, PA, 2nd ed edition, 2010. ISBN 9780443069529. (Cited on page 6)
- K. R. Foster and H. P. Schwan. Dielectric properties of tissues and biological materials: A critical review. *Critical reviews in biomedical engineering*, 17(1):25–104, 1989. (Cited on page 39)
- B. Frankenhaeuser. Sodium permeability in toad nerve and in squid nerve. *The Journal of Physiology*, 152:159–166, June 1960. (Cited on page 19)
- S. Gabriel, R. W. Lau, and C. Gabriel. The dielectric properties of biological tissues: III. Parametric models for the dielectric spectrum of tissues. *Physics in medicine and biology*, 41(11):2271–2293, Nov. 1996. (Cited on page 39)
- L. A. Geddes and L. E. Baker. The specific resistance of biological material—a compendium of data for the biomedical engineer and physiologist. *Medical & biological engineering*, 5(3):271–293, May 1967. (Cited on page 39)
- W. Y. Gu, M.-A. Justiz, and H. Yao. Electrical conductivity of lumbar anulus fibrosis: Effects of porosity and fixed charge density. *Spine*, 27(21):2390–2395, Nov. 2002. (Cited on page 39)
- S. Harkema, Y. Gerasimenko, J. Hodes, J. Burdick, C. Angeli, Y. Chen, C. Ferreira, A. Willhite, E. Rejc, R. G. Grossman, and V. R. Edgerton. Effect of epidural stimulation of the lumbosacral spinal cord on voluntary movement, standing, and assisted stepping after motor complete paraplegia: A case study. *Lancet*, 377(9781):1938–1947, June 2011. (Cited on page 1)

- T. Hasegawa, Y. Mikawa, R. Watanabe, and H. S. An. Morphometric analysis of the lumbosacral nerve roots and dorsal root ganglia by magnetic resonance imaging. *Spine*, 21(9):1005–1009, May 1996. (Cited on pages 11 and 13)
- A. L. Hodgkin and A. F. Huxley. A quantitative description of membrane current and its application to conduction and excitation in nerve. *The Journal of Physiology*, 117(4):500–544, Aug. 1952. (Cited on pages 16 and 19)
- U. Hofstoetter, C. Hofer, H. Kern, S. Danner, W. Mayr, M. Dimitrijevic, and K. Minassian. Neuromodulation of voluntary locomotor activity by transcutaneous spinal cord stimulation in motor-incomplete spinal cord injured individuals: A preliminary study. *Artif. Organs*, 2014a. (Cited on page 2)
- U. S. Hofstoetter, K. Minassian, C. Hofer, W. Mayr, F. Rattay, and M. R. Dimitrijevic. Modification of reflex responses to lumbar posterior root stimulation by motor tasks in healthy subjects. *Artificial Organs*, 32(8):644–648, Aug. 2008. (Cited on page 24)
- U. S. Hofstoetter, W. B. McKay, K. E. Tansey, W. Mayr, H. Kern, and K. Minassian. Modification of spasticity by transcutaneous spinal cord stimulation in individuals with incomplete spinal cord injury. *The Journal of Spinal Cord Medicine*, 37(2):202–211, Mar. 2014b. (Cited on page 2)
- J. Holsheimer. Computer modelling of spinal cord stimulation and its contribution to therapeutic efficacy. *Spinal cord*, 36(8):531–540, Aug. 1998a. (Cited on page 39)
- J. Holsheimer. Concepts and methods in neuromodulation and functional electrical stimulation: An introduction. *Neuromodulation: Technology at the Neural Interface*, 1(2):57–61, Apr. 1998b. (Cited on page 64)
- J. Holsheimer. Which neuronal elements are activated directly by spinal cord stimulation. *Neuromodulation: Journal of the International Neuromodulation Society*, 5(1):25–31, Jan. 2002. (Cited on page 24)
- J. Holsheimer, J. A. den Boer, J. J. Struijk, and A. R. Rozeboom. MR assessment of the normal position of the spinal cord in the spinal canal. *AJNR. American journal of neuroradiology*, 15(5):951–959, May 1994. (Cited on pages 2 and 62)
- J. Holsheimer, G. Barolat, J. J. Struijk, and J. He. Significance of the spinal cord position in spinal cord stimulation. *Acta Neurochirurgica. Supplement*, 64:119–124, 1995. (Cited on pages 2, 3 and 62)
- Judith Brown CPD. Neurological anatomy of the lower limb. URL <http://www.judithbrowncpd.co.uk/Neurologicalanatomyofthelowerlimb.pdf>. Last visited on 22.11.2014. (Cited on page 9)
- T. Kameyama, Y. Hashizume, and G. Sobue. Morphologic features of the normal human cadaveric spinal cord. *Spine*, 21(11):1285–1290, June 1996. (Cited on pages 36 and 37)

- E. R. Kandel, J. H. Schwartz, and T. M. Jessell. *Principles of neural science*. McGraw-Hill, Health Professions Division, New York, 4th edition, 2000. ISBN 0838577016. (Cited on page 15)
- M. Knikou. Neurophysiological characterization of transspinal evoked potentials in human leg muscles. *Bioelectromagnetics*, 34(8):630–640, Dec. 2013. (Cited on page 2)
- A. Kuhn. *Modeling Transcutaneous Electrical Stimulation*. Dissertation, ETH Zurich, 2008. (Cited on page 39)
- J. Ladenbauer. *Simulation of the Excitation of Human Lower Spinal Cord Structures with Surface Electrodes: 3D Finite Element Analysis and Nerve Fiber Modeling*. Master Thesis, Technische Universität Wien, Wien, Oct. 2008. (Cited on pages 1, 30, 39 and 62)
- J. Ladenbauer, K. Minassian, U. S. Hofstoetter, M. R. Dimitrijevic, and F. Rattay. Stimulation of the human lumbar spinal cord with implanted and surface electrodes: A computer simulation study. *IEEE Transactions on Neural Systems and Rehabilitation Engineering*, 18(6):637–645, Dec. 2010. (Cited on pages 2 and 23)
- J. Lang. Lendenwirbelsäulenerkrankungen mit Beteiligung des Nervensystems. In *Neuroorthopädie 2*. Springer Verlag, Berlin, 1984. (Cited on pages 11 and 42)
- J. Lang and U. Geisel. Lumbosacral part of the dural sac and the topography of its contents. *Morphologia medica*, 3(1):27–46, May 1983. (Cited on pages 10 and 42)
- K. Malinowsky. Maßbestimmungen am Wirbelkanal: Lage der einzelnen Teile und sonstige Verhältnisse desselben. In *Archiv für Anatomie*, pages 249–274. 1911. (Cited on pages 35 and 38)
- J. Malmivuo. *Bioelectromagnetism: Principles and applications of bioelectric and bio-magnetic fields*. Oxford University Press, New York, 1995. ISBN 0195058232. (Cited on page 39)
- C. C. McIntyre, A. G. Richardson, and W. M. Grill. Modeling the excitability of mammalian nerve fibers: Influence of afterpotentials on the recovery cycle. *Journal of Neurophysiology*, 87(2):995–1006, Feb. 2002. (Cited on pages 42, 44 and 45)
- D. R. McNeal. Analysis of a model for excitation of myelinated nerve. *IEEE Transactions on Biomedical Engineering*, BME-23(4):329–337, July 1976. (Cited on page 17)
- D. Miklavčič, N. Pavšelj, and F. X. Hart. Electric properties of tissues. In *Wiley Encyclopedia of Biomedical Engineering*. John Wiley & Sons, Inc., Hoboken, NJ, USA, Apr. 2006. ISBN 9780471740360. (Cited on page 39)
- K. Minassian. *Excitation of Lower Spinal Cord Structures with Implanted Electrodes: 3D Finite Element Analysis and Simulation of Neural Responses*. Master Thesis, Technische Universität Wien, Wien, May 2000. (Cited on pages 10, 11, 12 and 42)

- K. Minassian, B. Jilge, F. Rattay, M. M. Pinter, H. Binder, F. Gerstenbrand, and M. R. Dimitrijevic. Stepping-like movements in humans with complete spinal cord injury induced by epidural stimulation of the lumbar cord: Electromyographic study of compound muscle action potentials. *Spinal Cord*, 42(7):401–416, July 2004. (Cited on page 24)
- K. Minassian, I. Persy, F. Rattay, M. R. Dimitrijevic, C. Hofer, and H. Kern. Posterior root-muscle reflexes elicited by transcutaneous stimulation of the human lumbosacral cord. *Muscle & nerve*, 35(3):327–336, Mar. 2007. (Cited on pages 1, 2 and 24)
- K. Minassian, U. S. Hofstoetter, K. Tansey, F. Rattay, W. Mayr, and M. R. Dimitrijevic. Transcutaneous stimulation of the human lumbar spinal cord: Facilitating locomotor output in spinal cord injury. In *Neuroscience 2010*, San Diego, CA, 2010. Society for Neuroscience. (Cited on page 24)
- K. Minassian, U. Hofstoetter, and F. Rattay. Transcutaneous lumbar posterior root stimulation for motor control studies and modification of motor activity after spinal cord injury. In *Restorative neurology of spinal cord injury*, pages 226–255. Oxford University Press, New York, 2012. ISBN 9780199746507. (Cited on pages 23, 24, 25, 26 and 27)
- L. G. Nowak and J. Bullier. Axons, but not cell bodies, are activated by electrical stimulation in cortical gray matter. II. Evidence from selective inactivation of cell bodies and axon initial segments. *Experimental Brain Research*, 118(4):489–500, Feb. 1998. (Cited on page 16)
- J. C. Olin, D. H. Kidd, and R. B. North. Postural changes in spinal cord stimulation perceptual thresholds. *Neuromodulation: Journal of the International Neuromodulation Society*, 1(4):171–175, Oct. 1998. (Cited on page 2)
- R. Porter. Focal stimulation of hypoglossal neurones in the cat. *The Journal of Physiology*, 169:630–640, Dec. 1963. (Cited on page 16)
- V. Raicu, N. Kitagawa, and A. Irimajiri. A quantitative approach to the dielectric properties of the skin. *Physics in medicine and biology*, 45(2):L1–4, Feb. 2000. (Cited on page 39)
- J. B. Ranck. Which elements are excited in electrical stimulation of mammalian central nervous system: A review. *Brain Research*, 98(3):417–440, Nov. 1975. (Cited on page 16)
- M. R. B. Ranger, G. J. Irwin, K. M. Bunbury, and J. M. Peutrell. Changing body position alters the location of the spinal cord within the vertebral canal: A magnetic resonance imaging study. *British Journal of Anaesthesia*, 101(6):804–809, Dec. 2008. (Cited on pages 2 and 62)
- F. Rattay. Analysis of models for external stimulation of axons. *IEEE Transactions on Biomedical Engineering*, BME-33(10):974–977, Oct. 1986. (Cited on page 22)

- F. Rattay. Ways to approximate current-distance relations for electrically stimulated fibers. *Journal of Theoretical Biology*, 125(3):339–349, Apr. 1987. (Cited on page 16)
- F. Rattay. Analysis of models for extracellular fiber stimulation. *IEEE Transactions on Biomedical Engineering*, 36(7):676–682, July 1989. (Cited on page 22)
- F. Rattay. *Electrical nerve stimulation: Theory, experiments, and applications*. Springer Verlag, Wien ; New York, 1990. ISBN 9783211822470. (Cited on pages 16 and 18)
- F. Rattay. Analysis of the electrical excitation of CNS neurons. *IEEE Transactions on Biomedical Engineering*, 45(6):766–772, June 1998. (Cited on page 16)
- F. Rattay. The basic mechanism for the electrical stimulation of the nervous system. *Neuroscience*, 89(2):335–346, Mar. 1999. (Cited on pages 16, 19, 22 and 62)
- F. Rattay, K. Minassian, and M. R. Dimitrijevic. Epidural electrical stimulation of posterior structures of the human lumbosacral cord: 2. quantitative analysis by computer modeling. *Spinal cord*, 38(8):473–489, Aug. 2000. (Cited on page 39)
- F. Rattay, K. Minassian, F. Gerstandbrand, H. Binder, M. Pinter, and M. Dimitrijevic. Neurophysiologische Modellierung der Erregbarkeit der Lokomotionszentren im lumbalen Rückenmark durch elektrische Stimulation. Endbericht, Nov. 2002. URL <https://www.bmvit.gv.at/innovation/publikationen/biomedizinischetechnik/downloads/endbericht200212091.pdf>. Last visited on 24.08.2014. (Cited on page 2)
- F. Rattay, R. J. Greenberg, and S. Resatz. Neuron modeling. In *Handbook of neuroprosthetic methods*. CRC Press, Boca Raton, 2003. ISBN 9780849311000. (Cited on pages 16, 17, 18, 20 and 21)
- E. Ross and D. Abejón. Improving patient experience with spinal cord stimulation: Implications of position-related changes in neurostimulation. *Neuromodulation: Journal of the International Neuromodulation Society*, 17 Suppl 1:36–41, June 2014. (Cited on page 2)
- B. J. Roth. Mechanisms for electrical stimulation of excitable tissue. *Critical Reviews in Biomedical Engineering*, 22(3-4):253–305, 1994. (Cited on page 16)
- F. D. Roy, G. Gibson, and R. B. Stein. Effect of percutaneous stimulation at different spinal levels on the activation of sensory and motor roots. *Experimental Brain Research*, 223(2):281–289, Nov. 2012. (Cited on page 2)
- J. Salinas. Cross Section of the Spinal Cord. URL <http://homepage.psy.utexas.edu/homepage/class/Psy332/Salinas/Neuroanatomy/Slide5.GIF>. Last visited on 22.11.2014. (Cited on page 9)

- C. M. Schade, D. M. Schultz, N. Tamayo, S. Iyer, and E. Panken. Automatic adaptation of neurostimulation therapy in response to changes in patient position: Results of the Posture Responsive Spinal Cord Stimulation (PRS) Research Study. *Pain Physician*, 14(5):407–417, Oct. 2011. (Cited on page 2)
- H. Schmidt, F. Heuer, L. Claes, and H.-J. Wilke. The relation between the instantaneous center of rotation and facet joint forces - A finite element analysis. *Clinical biomechanics (Bristol, Avon)*, 23(3):270–278, Mar. 2008. (Cited on page 38)
- D. M. Schultz, L. Webster, P. Kosek, U. Dar, Y. Tan, and M. Sun. Sensor-driven position-adaptive spinal cord stimulation for chronic pain. *Pain Physician*, 15(1):1–12, Feb. 2012. (Cited on page 2)
- J. R. Schwarz and G. Eikhof. Na currents and action potentials in rat myelinated nerve fibres at 20 and 37 degrees C. *Pflügers Archiv: European Journal of Physiology*, 409(6):569–577, Aug. 1987. (Cited on page 19)
- J. R. Schwarz, G. Reid, and H. Bostock. Action potentials and membrane currents in the human node of Ranvier. *Pflügers Archiv: European Journal of Physiology*, 430(2):283–292, June 1995. (Cited on page 19)
- J. Struijk, J. Holsheimer, G. Barolat, J. He, and H. Boom. Paresthesia thresholds in spinal cord stimulation: A comparison of theoretical results with clinical data. *IEEE Transactions on Rehabilitation Engineering*, 1(2):101–108, June 1993a. (Cited on page 39)
- J. J. Struijk, J. Holsheimer, B. K. van Veen, and H. B. Boom. Epidural spinal cord stimulation: Calculation of field potentials with special reference to dorsal column nerve fibers. *IEEE transactions on bio-medical engineering*, 38(1):104–110, Jan. 1991. (Cited on page 39)
- J. J. Struijk, J. Holsheimer, G. G. van der Heide, and H. B. Boom. Recruitment of dorsal column fibers in spinal cord stimulation: Influence of collateral branching. *IEEE transactions on bio-medical engineering*, 39(9):903–912, Sept. 1992. (Cited on page 39)
- J. J. Struijk, J. Holsheimer, and H. B. Boom. Excitation of dorsal root fibers in spinal cord stimulation: A theoretical study. *IEEE transactions on bio-medical engineering*, 40(7):632–639, July 1993b. (Cited on page 16)
- Z. Szava. *Three-dimensional finite element simulation of the electrical field distribution within the vertebral canal generated by surface electrodes*. Master Thesis, University of Applied Sciences Technikum Wien, Vienna, Austria, 2006. (Cited on page 39)
- P. Veltink, J. Van Alste, and H. Boom. Simulation of intrafascicular and extraneural nerve stimulation. *IEEE Transactions on Biomedical Engineering*, 35(1):69–75, Jan. 1988. (Cited on page 16)

E. J. Wall, M. S. Cohen, J. J. Abitbol, and S. R. Garfin. Organization of intrathecal nerve roots at the level of the conus medullaris. *The Journal of bone and joint surgery. American volume*, 72(10):1495–1499, Dec. 1990. (Cited on pages 10, 11 and 42)

WestOne Services. The polarised neuron (resting neuron). URL http://tle.westone.wa.gov.au/content/file/969144ed-0d3b-fa04-2e88-8b23de2a630c/1/human_bio_science_3b.zip/content/002_nervous_control/page_10.htm. Last visited on 22.11.2014. (Cited on page 14)

Appendix

Listing A.1: code/extract.m

```
1 %Converts voxel data to point cloud
2 clear
3 clc
4
5 file_read = 'Duke_34y_V5_0.5mm.raw';
6 filename_write = 'Duke_34y_V5_0.5mm_muscle_';
7 fileext_write = '.csv';
8
9 nx = 1220;
10 ny = 620;
11 nz = 3720;
12
13 dx = 0.0005;
14 dy = 0.0005;
15 dz = 0.0005;
16
17 threshold = cast(48, 'char');
18 object_segmentation=false;
19
20 extracted=false(nx,ny,nz);
21 fid = fopen(file_read);
22 counter=0;
23
24 min_x=nx;
25 max_x=0;
26 min_y=ny;
```

```

27 max_y=0;
28
29 first_z=true;
30
31 for z=1:nz
32     clc
33     disp(['Reading: ' num2str(ceil((z/nz)*100)) '%'])
34
35     indices=find(fscanf(fid, '%c', nx*ny) == threshold);
36
37     if length(indices) > 1
38         if ~first_z
39             max_z = z;
40         else
41             min_z = z;
42             first_z = false;
43         end
44
45         for k = 1:length(indices)
46             x = mod(indices(k)-1,nx)+1;
47             y = mod(floor((indices(k)-1)/nx),ny)+1;
48             min_x = min([x min_x]);
49             min_y = min([y min_y]);
50             max_x = max([x max_x]);
51             max_y = max([y max_y]);
52             extracted(x,y,z) = true;
53             counter = counter + 1;
54         end
55     end
56 end
57
58 fclose(fid);
59
60 disp('Reducing Array Size')
61 extracted=extracted(min_x-1:max_x+1,min_y-1:max_y+1,min_z-1:
    max_z+1);
62
63 segments=1;
64
65 if object_segmentation
66     clc
67     disp('Segmenting')
68     [segmented,segments]= bwlabeln(extracted,6);

```

```

69 end
70
71
72 for i=1:segments
73     result{i}=zeros(counter,3);
74     counter2(i)=1;
75 end
76
77 for z=2:max_z-min_z
78     clc
79     disp(['Writing Positions: ' num2str(ceil(((z-1)/(max_z-
80         min_z))*100)) '%'])
81     for y=2:max_y-min_y
82         for x=2:max_x-min_x
83             if extracted(x,y,z) && (~extracted(x+1,y,z) || ~
84                 extracted(x-1,y,z) || ~extracted(x,y+1,z) || ~
85                 extracted(x,y-1,z) || ~extracted(x,y,z+1) || ~
86                 extracted(x,y,z-1))
87                 if object_segmentation
88                     segment_number = segmented(x,y,z);
89                 else
90                     segment_number = 1;
91                 end
92                 result{segment_number}(counter2(segment_number)
93                     ,:)=[(x-1)*dx (y-1)*dy (z-1)*dz];
94                 counter2(segment_number) = counter2(
95                     segment_number)+1;
96             end
97         end
98     end
99 end
100
101 for i=segments:-1:1
102     if counter2(i) < (nx*ny*nz)/100000
103         result(i)=[];
104         counter2(i)=[];
105     else
106         result{i} = result{i}(1:counter2(i)-1,:);
107     end
108 end
109
110 disp('Writing Results')

```

```

106 for i=1:length(result)
107     csvwrite([filename_write num2str(i) fileext_write], result{
        i})
108 end
109 disp('Finished')

```

Listing A.2: code/current.m

```

1 model = mphload('C:\Users\Deathy\Documents\Duke\
    solidworks2_back.mph');
2
3 oNames = model.geom('geom1').objectNames();
4
5 upDown = model.geom('geom1').getUpDown;
6
7 upDown = int32(upDown');
8
9 domain = cell(1,length(upDown));
10
11 for i = 1:length(domain)
12
13 domain{upDown(i,2)} = cat(2,domain{upDown(i,2)},i);
14
15 end
16
17 ccsf=mphint2(model,'abs((nx*ec.Jx)+(ny*ec.Jy)+(nz*ec.Jz))','
    surface','selection',domain{33,36});
18
19 cbe=mphint2(model,'abs((nx*ec.Jx)+(ny*ec.Jy)+(nz*ec.Jz))','
    surface','selection',[58,626]);
20
21 rcurrent_normal=((ccsf)/2)/cbe

```

Listing A.3: code/extract_sketch.bas

```

1 Attribute VB_Name = "Macro11"
2 Sub main()
3     Dim swApp As SldWorks.SldWorks
4     Dim doc As SldWorks.ModelDoc2
5     Dim part As SldWorks.PartDoc
6     Dim sm As SldWorks.SelectionMgr
7     Dim feat As SldWorks.feature
8     Dim sketch As SldWorks.sketch
9     Dim sPath As String: sPath = "C:\"
10

```

```

11  Set swApp = GetObject(, "sldworks.application")
12  If swApp Is Nothing Then
13      End
14  End If
15
16  Set doc = swApp.ActiveDoc
17  If doc Is Nothing Then
18      End
19  End If
20
21  If doc.GetType <> swDocPART Then
22      End
23  End If
24
25  Set part = doc
26  Set sm = doc.SelectionManager
27
28  If part Is Nothing Or sm Is Nothing Then
29      End
30  End If
31
32  If sm.GetSelectedObjectType2(1) <> swSelSKETCHES Then
33      MsgBox "No sketch selected"
34      End
35  End If
36
37  Set feat = sm.GetSelectedObject4(1)
38  Set sketch = feat.GetSpecificFeature
39
40  If sketch Is Nothing Then
41      End
42  End If
43
44  Dim fFile As String
45  Dim FileNumber As Long
46
47  fFile = sPath & feat.Name & ".csv"
48  FileNumber = FreeFile
49  Open fFile For Output As #FileNumber
50
51  'Write lines to file
52  If sketch.GetLineCount > 0 Then
53      lines = sketch.GetLines

```

```

54         got_line = False
55
56     For i = LBound(lines) To UBound(lines)
57         If Not got_line Then
58             points = lines(i)
59             current_points = 0
60             got_line = True
61             Print #FileNumber, "2" & ", " & CStr(points) &
                ", 0"
62         Else
63             Print #FileNumber, Line(lines(i), lines(i + 1),
                lines(i + 2))
64             i = i + 2
65             current_points = current_points + 1
66         End If
67
68         If current_points = points Then
69             got_line = False
70         End If
71     Next i
72 End If
73
74 'Write splines to file
75 If sketch.GetSplineCount(100000) > 0 Then
76     v = sketch.GetSplines
77     got_spline = False
78
79     For i = LBound(v) To UBound(v)
80         If Not got_spline Then
81             points = v(i + 2)
82             current_points = 0
83             got_spline = True
84             Print #FileNumber, "1" & ", " & CStr(points) &
                ", 0"
85             i = i + 2
86         Else
87             Print #FileNumber, Line(v(i), v(i + 1), v(i +
                2))
88             i = i + 2
89             current_points = current_points + 1
90         End If
91
92         If current_points = points Then

```



```

93         got_spline = False
94     End If
95     Next i
96 End If
97
98 Close #FileNumber
99 End Sub
100
101 Function Line(ByVal Value1 As Double, ByVal Value2 As Double,
    ByVal Value3 As Double) As String
102     Line = Replace(CStr(Value1), ",", ".") & ", " & Replace(
        CStr(Value2), ",", ".") & ", " & Replace(CStr(Value3), "
        , ",", ".")
103 End Function

```

Listing A.4: code/splines.m

```

1 clear
2 e = 0.0000001;
3 max_distance = 0.1;
4 hold on
5
6 %# absolute tolerance equality
7 isequalAbs = @(x,y,tol) ( not(ismember(0, abs(x-y) <= tol)) );
8
9 %# relative tolerance equality
10 isequalRel = @(x,y,tol) ( not(ismember(0, abs(x-y) <= ( tol*max
    (abs(x),abs(y)) + eps))) );
11
12 d = uigetdir(pwd, 'Select a folder');
13 files = dir(fullfile(d, '*.csv'));
14 delete(strcat(d, '\*.txt'));
15 fid = fopen(strcat(d, '\list.txt'),'a');
16
17 for z=1:length(files)
18     clearvars -except d files max_distance e pointcloud z
19     isequalRel isequalAbs fid
20     M = csvread(strcat(d, '/', files(z).name));
21     filename = strrep(files(z).name, ' ', '_');
22     i=1;
23     points={};
24
25     % Write each element into a separate cell, 1=spline, 2=line
26     while i<size(M,1)

```

```

26         points{end+1,1} = M(i+1:i+M(i,2),:);
27         points{end,2} = M(i,1);
28
29         i=i+M(i,2)+1;
30     end
31
32     % Check each element for connections to other elements
33     for i=1:size(points,1)
34         first=points{i,1}(1,:);
35         last=points{i,1}(end,:);
36         for j=1:size(points,1)
37             if j~=i
38                 other_first = points{j,1}(1,:);
39                 other_last = points{j,1}(end,:);
40
41                 if isequalAbs(other_first, first,e) ||
42                     isequalAbs(other_last, first,e)
43                     points{i,3} = j;
44                 end
45                 if isequalAbs(other_first, last,e) ||
46                     isequalAbs(other_last, last,e)
47                     points{i,4} = j;
48                 end
49             end
50         end
51     end
52
53     % Sort by connections to get 1 continuous line
54     count=2;
55     if size(points,1)==1
56         sorted_points{1,1}=points{1,1};
57         sorted_points{1,2}=points{1,2};
58     else
59         for i=1:size(points,1)
60             if isempty(points{i, 3}) || isempty(points{i, 4})
61                 sorted_points{1,1}=points{i,1};
62                 sorted_points{1,2}=points{i,2};
63
64                 if isempty(points{i, 3})
65                     next = points{i, 4};
66                 else
67                     next = points{i, 3};
68                 end

```

```

67
68         previous = i;
69
70         for j=1:size(points,1)
71             sorted_points{count,1} = points{next,1};
72             sorted_points{count,2} = points{next,2};
73
74             if not(isempty(points{next,3})) && points{next
75                 ,3} ~= previous
76                 previous = next;
77                 next = points{next,3};
78             elseif not(isempty(points{next,4})) && points{
79                 next,4} ~= previous
80                 previous = next;
81                 next = points{next,4};
82             else
83                 break;
84             end
85
86             count=count+1;
87         end
88     end
89     break
90 end
91
92 for i=1:size(sorted_points,1)
93     clear CS
94     %scatter3(sorted_points{i,1}(:,1),sorted_points{i
95         ,1}(:,2),sorted_points{i,1}(:,3));
96     CS = cat(1,0,cumsum(sqrt(sum(diff(sorted_points{i
97         ,1},[],1).^2,2))));
98     %sorted_points{i,1} = interp1(CS, sorted_points{i,1},
99         unique([CS(:)' 0:max_distance:CS(end) CS(end)]),'
100         cubic');
101     sorted_points{i,1} = interp1(CS, sorted_points{i,1},
102         unique([0:max_distance:CS(end)]),'cubic');
103 end
104
105 % Add all points to one vector and remove all duplicates
106 pointcloud{z} = sorted_points{1,1};
107 for i=2:size(sorted_points,1)

```

```

102         pointcloud{z} = vertcat(pointcloud{z}, sorted_points{i
            ,1});
103     end
104     pointcloud{z}=unique(pointcloud{z},'rows','stable');
105     plot3(pointcloud{z}(:,1),pointcloud{z}(:,2),pointcloud{z}
            (:,3));
106
107     fprintf(fid, '%s %u\n', filename, size(pointcloud{z},1));
108     dlmwrite(strcat(d,'/',filename,'.txt'),pointcloud{z},'
            delimiter',' ','precision', 10);
109     dlmwrite(strcat(d,'/','all_points.txt'),pointcloud{z}, '-
            append','delimiter',' ','precision', 10);
110 end
111
112 fclose(fid);
113
114 axis equal

```

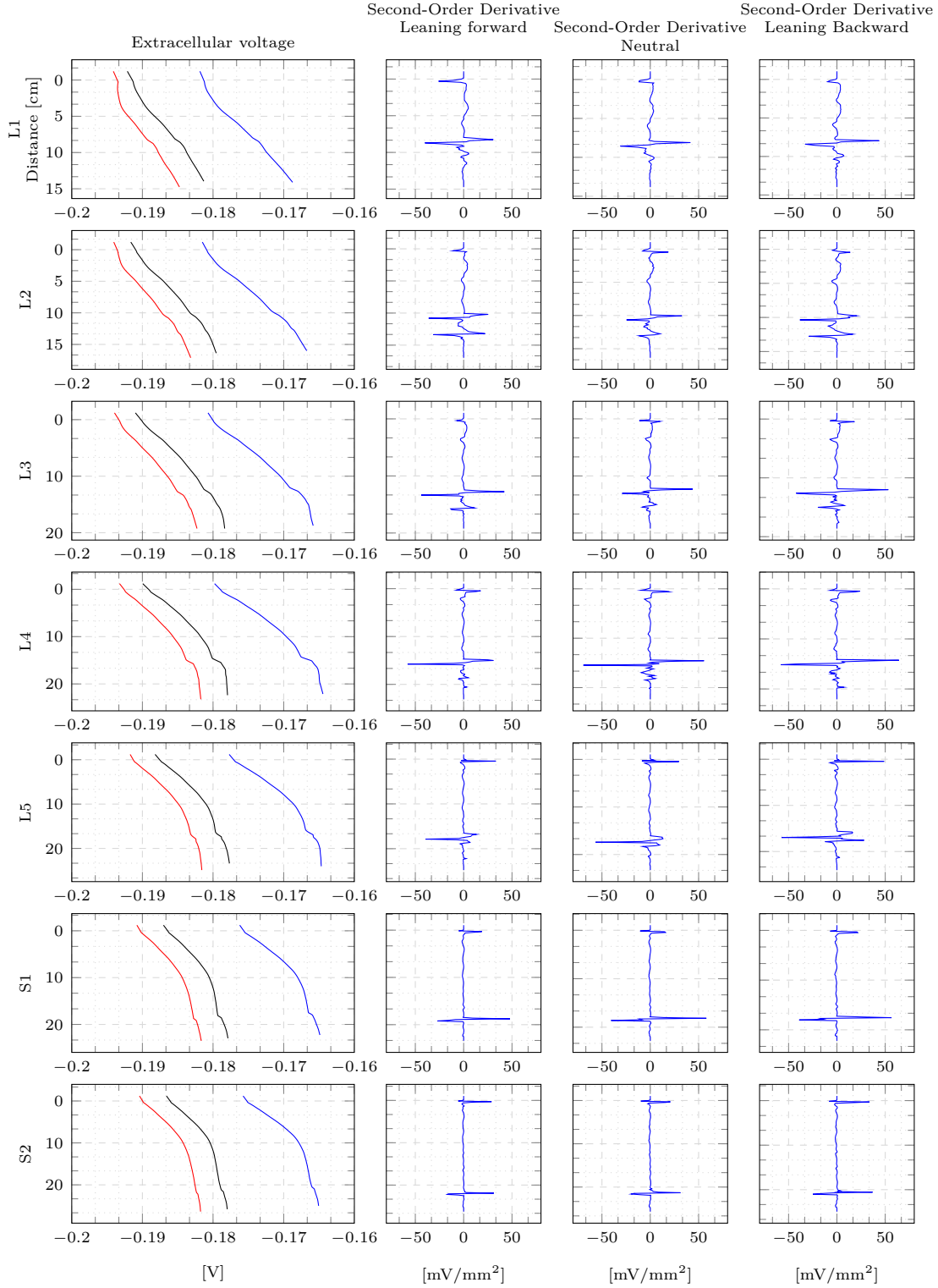


Figure A.1: Extracellular voltage and its second-order derivative of the right anterior roots in different positions. Colors of the curves in the extracellular voltage diagram indicate the position: **leaning forward**, upright, **leaning backward**.

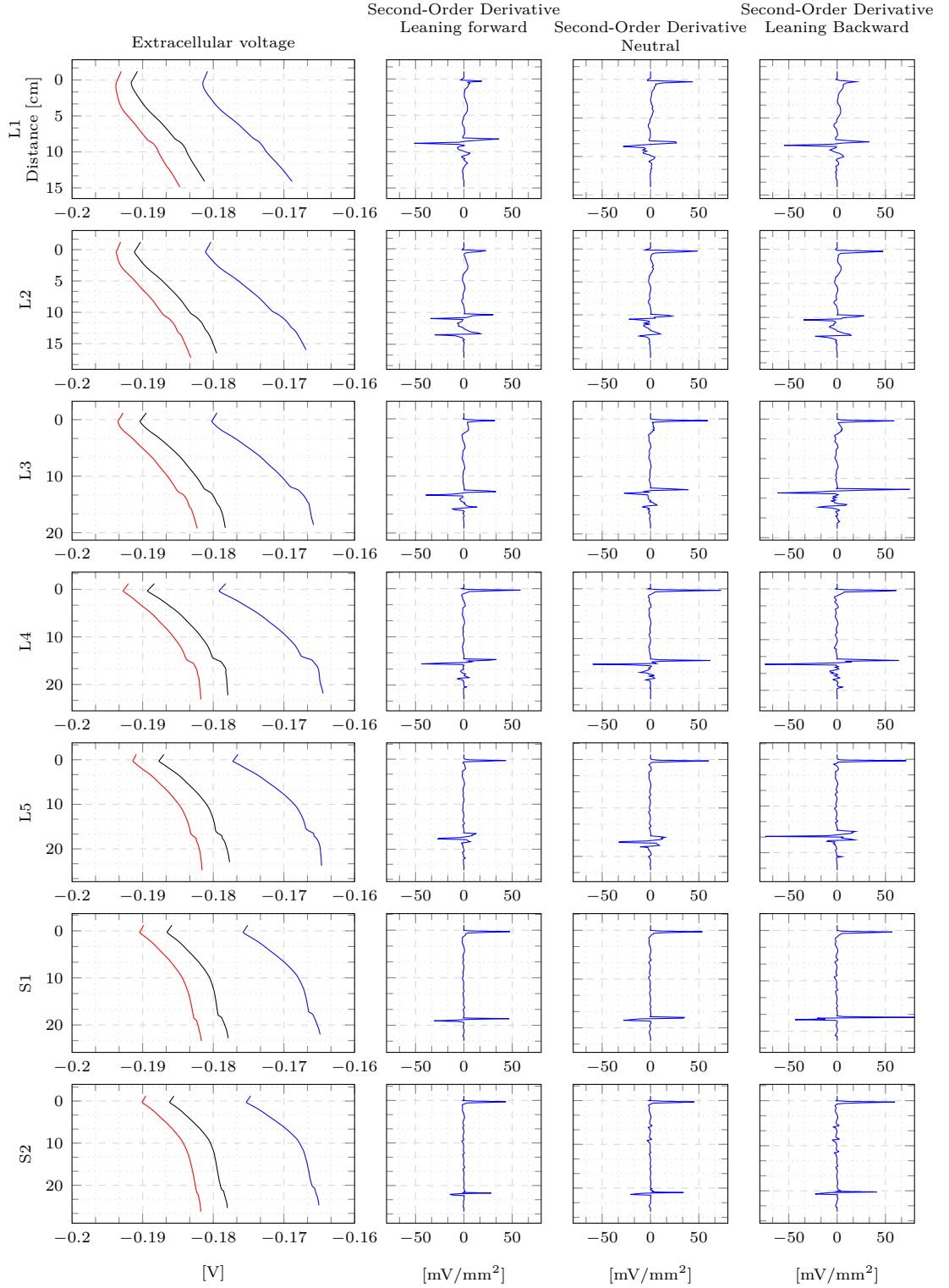


Figure A.2: Extracellular voltage and its second-order derivative of the right posterior roots in different positions. Colors of the curves in the extracellular voltage diagram indicate the position: **leaning forward**, upright, **leaning backward**.